

THESIS FOR THE DEGREE OF DOCTOR OF PHILOSOPHY

**Microscopy of high temperature oxidation of iron
and some stainless steels**

TORBJÖRN JONSSON

Department of Applied Physics
CHALMERS UNIVERSITY OF TECHNOLOGY
Göteborg, Sweden 2007

Microscopy of high temperature oxidation of iron and some stainless steels

Torbjörn Jonsson

© TORBJÖRN JONSSON, 2007

ISBN 978-91-7291-914-3

Doktorsavhandlingar vid Chalmers tekniska högskola

Ny serie nr 2595

ISSN 0346-718X

Department of Applied Physics
Chalmers University of Technology
SE-412 96 Göteborg
Sweden
Telephone + 46 (0)31-772 1000

Cover: FIB image showing an ion milled cross-section of iron oxide formed on pure iron after 24 hours exposure in dry oxygen. The sample is tilted 40° and the total thickness of the layered oxide scale is about 20 μm . A duplex magnetite (Fe_3O_4) layer can be seen below a thinner hematite (Fe_2O_3) layer.

Chalmers Reproservice
Göteborg, Sweden 2007

Microscopy of high temperature oxidation of iron and some stainless steels

Torbjörn Jonsson
Department of Applied Physics
Chalmers University of Technology

Abstract

This thesis concerns the high temperature oxidation of iron and some stainless steels. The oxide scales, as well as the subjacent metal, were investigated using a range of electron and ion microscopy techniques, including SEM, TEM, EDX and FIB. The aim was to link the microstructural observations to the oxidation mechanisms of the materials.

It was shown that iron exposed to O_2 with 100 ppm SO_2 forms a thinner more dense oxide scale than iron exposed in pure O_2 . The oxide scales consisted of two magnetite layers below a hematite layer. The inhibitive effect is attributed to the presence of iron sulphide that blocks active sites on the hematite surface, slowing down the formation of oxygen ions.

The impact of water vapour was studied on the oxidation of iron, the ferritic/martensitic stainless steel X20 and on the austenitic stainless steel 353MA. Iron oxidation was studied through an ESEM *in-situ* investigation at 500 °C. Several factors are suggested to influence the local oxide growth rate of iron: (i) the surface of the metal grain, (ii) the thickness of the hematite layer, (iii) the oxide grain size, and (iv) the exposure environment. The two alloys sometimes experience breakaway oxidation in O_2/H_2O mixtures, because their oxide scales are depleted in Cr due to the formation of $CrO_2(OH)_2(g)$. The transition from a thin protective Cr-rich oxide scale to non-protective Fe-rich oxide scale is faster, *i.e.* the entire surface is covered with thick oxide within a short time after the initiation of breakaway oxidation, for the ferritic/martensitic stainless steel than for a typical austenitic stainless steel. This can be attributed to the higher bulk diffusion rate and the higher density of faster diffusion paths (steel grain boundaries). Alloy 353MA, exposed at 700 °C, forms a Cr-rich healing layer beneath the Fe-rich oxide some time after breakaway oxidation. It is suggested to be a result of the high Cr/Fe ratio of the alloy. The behavior at 900 °C was different. In spite of the loss of Cr from the oxide scale, breakaway oxidation did not occur. This is suggested to be a combined effect of more rapidly chromium diffusion, spinels formed at the oxide/gas interface and the high Ni content in the alloy.

The influence of KCl on the initial breakdown of the protective scale on the austenitic stainless steel 304L was studied in dry and wet oxygen at 600 °C. The rapid breakdown of the protective scale is suggested to be caused by the formation of K_2CrO_4 , depleting the protective oxide in chromium. Cl is suggested to play a minor role in the initial breakdown of the protective scale.

Keywords: High-temperature oxidation, water vapour, sulphur dioxide, KCl, stainless steel, iron, 353MA, X20, microstructure, SEM, TEM, EDX, FIB, FIB/SEM, *in-situ* ESEM

PREFACE

This thesis covers the research conducted at the Microscopy and Microanalysis group at the Department of Applied Physics, Chalmers University of Technology, Sweden during the period 2003-2007 under the supervision of Associated Professor Mats Halvarsson. The work was carried out within the High Temperature Corrosion (HTC) centre and the Swedish Foundation for Strategic Research (SSF) Materials Research Programme “Mechanisms of creep and oxidation of high performance alloys” (CROX).

List of appended papers:

- I. **The effect of traces of SO₂ on iron oxidation:
A microstructural study**
T. Jonsson, A. Järtnäs, J. –E. Svensson, L. –G. Johansson and M. Halvarsson
Oxidation of Metals, 2007. 67(3-4): p. 193-213
- II. **An ESEM *in-situ* investigation of the influence of H₂O on iron oxidation at 500°C.**
T. Jonsson, B. Pujilaksono, S. Hallström, J. Ågren, J. –E. Svensson, L. –G. Johansson and M. Halvarsson
Submitted to Corrosion Science
- III. **Microstructure Investigation of Protective and Non-Protective Oxides on 11% Chromium Steel**
F. Liu, J. E. Tang, T. Jonsson, S. Canovic, K. Segerdahl, J. –E. Svensson, and M. Halvarsson
Oxidation of Metals, 2006. 66(5/6): p. 295-319
- IV. **Microstructural investigation of the effect of water vapour on the oxidation of alloy 353MA in oxygen at 700 and 900°C**
T. Jonsson, S. Canovic, F. Liu, H. Asteman, J. –E. Svensson, L. –G. Johansson and M. Halvarsson
Materials at High Temperature, 2005. 22(3-4): p. 231-243
- V. **Microstructural investigation of the effect of water vapour on the oxidation of the Si-containing FeCrNi steel 353MA at 900°C in oxygen**
T. Jonsson, F. Liu, S. Canovic, H. Asteman, J. –E. Svensson, L. –G. Johansson and M. Halvarsson
Submitted to Journal of The Electrochemical Society

- VI. **The influence of KCl on the corrosion of an austenitic stainless steel (304L) in oxidizing humid conditions at 600°C: A microstructural study**
T. Jonsson, J. Froitzheim, J. Pettersson, J. -E. Svensson, L. -G. Johansson and M. Halvarsson
Submitted to Oxidation of Metals
- VII. **Microstructural investigation of the influence of KCl on the corrosion of 304L exposed to 5% O₂ + N₂**
T. Jonsson, J. Froitzheim, J. Pettersson, J. -E. Svensson, L. -G. Johansson and M. Halvarsson
16th International Corrosion Congress. 2005. Beijing, China, Paper Number 6-45

List of related papers:

The following papers and KME report have also been produced during this time but are not appended since they are not within the scope of this thesis.

- A. **Oxidation behaviour of a (Mo,W)Si₂ based composite in dry and wet oxygen atmospheres in the temperature range 350-950°C**
K. Hansson, J. E. Tang, T. Jonsson, M. Halvarsson, R. Pompe, M. Sundberg and J. -E. Svensson.
Submitted to Journal of the European Ceramic Society
- B. **KME-132 Material evaluation and research in the waste fired boiler at Händelö.**
Skog, E., S. Hansson, *et al.*
KME report 2004
- C. **High Resolution Chemical Analysis in SEM**
T. Jonsson, S. Canovic, F. Liu and M. Halvarsson
The 16th International Microscopy Congress (IMC16). 2006. Sapporo, Japan
- D. **Microstructural investigation of chips formed during metal cutting**
S. Canovic, T. Jonsson, S. Rупpi and M. Halvarsson
The 16th International Microscopy Congress (IMC16). 2006. Sapporo, Japan

*Torbjörn Jonsson
Göteborg, May 2007*

Table of contents

Chapter 1	Introduction	1
1.1	General	1
1.2	Background	1
1.3	Aim	2
Chapter 2	Iron and stainless steels	5
2.1	Iron	5
2.2	Stainless steels	6
Chapter 3	Oxidation mechanisms	11
3.1	General	11
3.2	Oxides	14
3.3	Oxidation of stainless steels	18
3.4	Previous studies	19
Chapter 4	Experimental techniques	23
4.1	Exposures	24
4.2	Scanning electron microscope (SEM)	26
4.3	Environmental scanning electron microscope (ESEM)	29
4.4	Focused ion beam (FIB) workstation	30
4.5	FIB/SEM workstation	33
4.6	Transmission electron microscope (TEM)	33
4.7	Specimen preparation	35
4.8	Complementary experimental techniques	40
Chapter 5	Result and discussion	43
5.1	Summary of appended papers	43
5.2	Results from work in progress	47
5.3	Future work	50
	Acknowledgements	52
	References	53

Chapter 1

Introduction

1.1 General

High temperature corrosion is an important degradation process in many industrial applications. It limits the lifetime of materials and restricts fuels for processes and systems. In order to predict the oxidation behaviour for a material in high temperature applications it is essential to understand how various species in the environment affects the material. It is therefore important to study the mechanisms behind high temperature corrosion in order to understand and hopefully prevent or retard the degradation. The link between microstructure evolution and exposure conditions can be used to comprehend the impact on the oxidation mechanisms of different species, common in high temperature applications. In this thesis analytical electron and ion microscopy has been used to investigate the microstructure of some metals and their oxide scales.

1.2 Background

One of the applications where high temperature corrosion plays an important role is in power plants. When fuels are burnt for production of electrical energy, hot combustion gases are produced. Under these conditions, corrosion becomes a problem. Many important components, such as boilers, steam generators, turbines etc. can be damaged by the corrosion process. This is why high temperature corrosion is an important issue in energy production.

One way of controlling the corrosion is to decrease the operating temperature. However, this results in decreased efficiency, which is not desirable. The aim for the thermal power plants is instead to increase, not reduce, the operating temperature in order to improve the efficiency.

A common way of improving the corrosion resistance is to use more highly alloyed stainless steels, such as for example 304L, Sanicro 28 or 353MA. These materials are, however, generally much more expensive than the low alloyed steels. A third way to control the corrosion of parts exposed to the combustion gas in a power plant is by additions to the fuel, thereby creating a less corrosive combustion gas. In order to do so a basic understanding about how the corrosion mechanisms are affected by different components of the combustion gas is needed.

Fireside corrosion is greatly influenced by the type of fuel used. Two gas components that are common in many types of fuels are H₂O and SO₂. Water vapor is often one of the main gas components together with N₂, O₂ and CO₂, while SO₂ typically appears in smaller amounts [1]. If renewable fuels, *e.g.* straw or wood chips, are used the gas typically contains alkali chlorides (*e.g.* KCl) and hydrochloric acid in addition to the other species [1].

The Swedish competence centre for the study of high temperature corrosion (HTC) hosts a number of research projects aimed at understanding corrosive behaviour of materials in different environments. The work performed within the scope of this thesis was partly carried out within HTC and partly within the Swedish Foundation for Strategic Research (SSF) Materials Research Programme “Mechanisms of creep and oxidation of high performance alloys” (CROX). The work performed within the HTC addresses the influence of common species in fireside corrosion, *e.g.* SO₂, H₂O and KCl, on high temperature corrosion while the work performed within SSF programme addresses the oxidation on a more fundamental level. Pure metals and model alloys were therefore investigated within the SSF programme in order to increase the fundamental understanding and in addition to give input to modelling of the oxidation behavior.

1.3 Aim

The work described in this thesis investigates the effect of different species in the environment, *i.e.* O₂, SO₂, H₂O and KCl. All species are common in fireside corrosion and the influences of these species are investigated on iron and different stainless steels. The microstructure and chemical composition of the oxide scales and the subjacent metal were investigated on samples exposed with and without these species. The detailed information about the influence on the microstructure of these species was combined with oxidation kinetics and other types of characterization of the corrosion products, mainly by X-ray diffraction (XRD), acquired by collaborators at the Department of Chemical and Biological Engineering at Chalmers University of Technology. The aim is to gain a fundamental understanding about the oxidation process through detailed studies of the carefully exposed samples.

Low levels of sulphur dioxide in the environment have been shown to give a lower oxidation rate on some metals and alloys [2]. The influence of low levels of sulphur dioxide was therefore investigated on pure iron at 500 °C (Paper I) and the aim was to understand the influence of sulphur dioxide on the oxidation.

The presence of water vapour is generally known to increase the corrosivity of the environment at high temperatures. The effect of water vapour was investigated on iron and two different stainless steels. The influence of water vapour on the initial oxidation of iron was investigated in Paper II. Two structurally different stainless steels were investigated, *i.e.* the ferritic/martensitic stainless steel X20 (Paper III) and the highly alloyed austenitic stainless steel 353MA (Paper IV and V). The aim was to better understand the impact of water vapour in the environment and the effect of the steel microstructure. These results can in addition be compared with the results from earlier investigations of other stainless steels. In particular, the oxidation behavior of the 304-type austenitic steels has been analyzed extensively [3, 4].

The presence of alkali chlorides has been shown to increase the corrosion rate of stainless steels [5-8]. In this thesis the effect of small additions KCl(s) were studied in wet and dry atmospheres (Paper VI and VII). Especially, the initial breakdown of the protective scale was studied. The influence of KCl(s) was investigated on the austenitic stainless steel 304-type.

Chapter 2

2

Iron and stainless steels

Both the composition and the microstructure of an alloy will determine its high temperature corrosion resistance. Important characteristics of iron and stainless steels will therefore be presented in this chapter. A short overview of stainless steels will in addition be given.

2.1 Iron

Oxidation of iron in oxygen has been extensively studied and is relatively well characterized. Iron is therefore good to use in order to investigate the influence of different species in the atmosphere on the oxidation behavior. This is the reason why the effect of O_2/H_2O mixtures and low levels of SO_2 has been studied on iron. Pure iron is however hard to produce, which is the reason why iron typically contains traces of other elements. The iron used in this work is of high quality and only contains some traces of other elements, see composition in Papers I and II.

Iron is the basis for all steels even though some highly alloyed stainless steels can contain high levels of other alloying elements. Iron exists in two crystal forms in atmospheric pressure. They are the body centered cubic (bcc) structure called α -iron, which exists below 910 °C, and the face centered cubic (fcc) structure called γ -iron, which exists above 910 °C. The bcc structure [Fig. 2.1] is more loosely packed than the fcc structure [Fig. 2.2]. This results in a higher diffusion rate in the bcc structure than in the fcc structure. All the iron samples used in this work have been used at a temperature well below the α - γ iron transition temperature 910 °C, *i.e.* only α -iron has been used. Pure iron is however extremely weak and corrosive, which explains the additions of other alloying elements to create (stainless) steels.

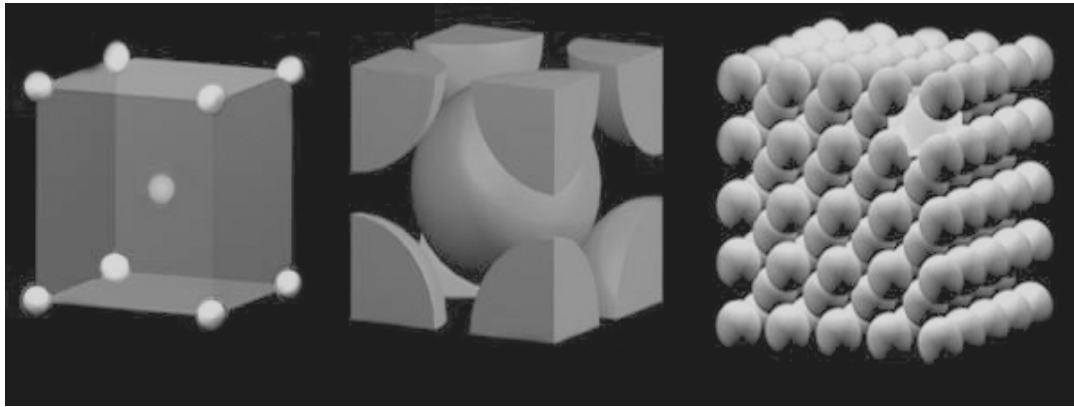


Figure 2.1: *The crystal structure of α -iron (BCC).*

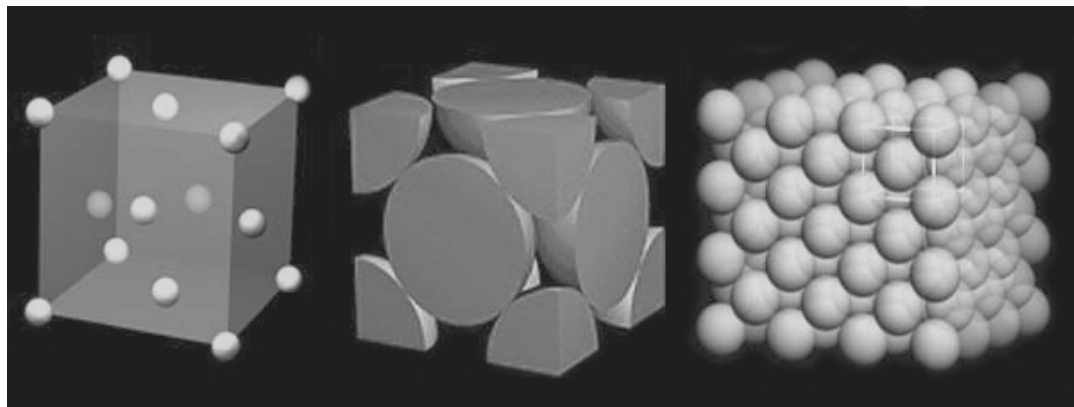


Figure 2.2: *The crystal structure of γ -iron (FCC).*

2.2 Stainless steels

The addition of carbon to iron forms one of the most common construction material used in industry: steel. The addition of carbon to iron improves important properties such as toughness and hardness. However, from a corrosion point of view, low-alloyed steels are very poor since they corrode in air and other important environments. In order to achieve better corrosion resistance another group of iron-based steels has been developed: stainless steels. The good mechanical properties combined with good corrosion resistance make these steels very important. The research of stainless steels is an important field and even though a lot of research has been done work still remains before a more complete understanding of their properties can be achieved.

As their name indicates, stainless steels have a high corrosion resistance, which is one of the reasons for their widespread use. The good corrosion resistance is caused by the formation of an adherent, thin and protective oxide film on the surface, which covers the metal. As Cr is added to the steel, a stabilization of the corrosion rate is achieved at about 10 wt.% Cr, which is caused by the formation of a protective Cr-rich oxide on the surface. This ability to form a protective oxide film on the surface in oxidizing environments makes Cr the most important alloying element in stainless steels.

According to their microstructure, stainless steels can be divided into four groups: martensitic (body-centered tetragonal or cubic), ferritic (bcc), austenitic (fcc) and duplex stainless steels (a combination of ferrite and austenite) [9]. In order to understand the microstructure and thereby the properties of stainless steels it is important to understand the effect of the different alloying elements on the microstructure.

Wever stated that the iron-carbon binary equilibrium system could be divided into four categories [9]: open and closed γ -field system, and expanded and contracted γ -field systems [Fig. 2.3]. This means that the different alloying elements can influence the equilibrium diagram in two ways:

- (a) by expanding the γ -field, and encouraging the formation of austenite over wider compositional limits. These elements (*e.g.* Ni and Mn) are called γ -stabilizers.
- (b) by contracting the gamma γ -field, and encouraging the formation of ferrite over wider compositional limits. These elements (*e.g.* Cr and Si) are called α -stabilizers.

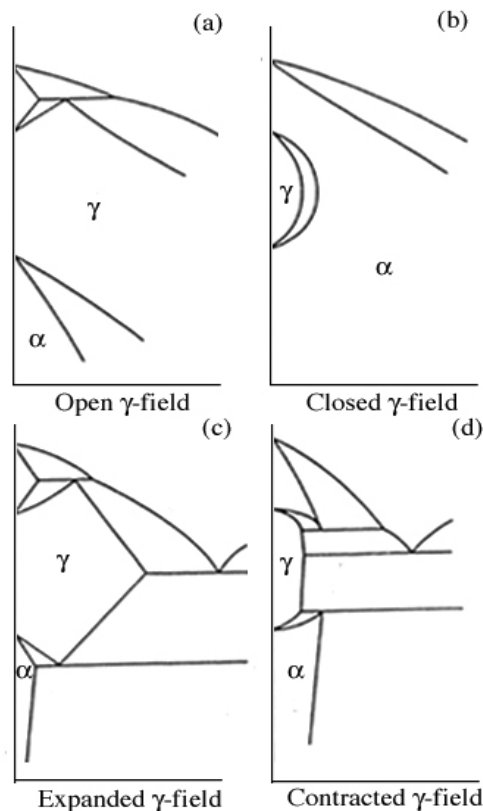


Figure 2.3: Classification of the iron alloy phase diagrams: (a) open γ -field; (b) closed γ -field; (c) expanded γ -field; (d) contracted γ -field [9].

The addition of different alloying elements determines the microstructure and thereby the properties of the alloy. In this thesis austenitic (304L, 353MA) and ferritic/martensitic (X20) stainless steels have been investigated. Other important features of the microstructure are the steel grain size and the presence of precipitates. The focus of this thesis is however on the oxidation of these stainless steels and only on how the microstructure of the bulk influences the oxidation behavior.

2.2.1 Ferritic stainless steels

Ferritic stainless steels are iron-based steels that contain between 17 and 30 wt.% Cr [9]. The structure of the ferritic stainless steels is relatively simple. They consist of a Cr-Fe solid solution, which has a bcc crystal structure, see Fig. 2.1. These steels have good corrosion resistance in many environments, especially at high Cr levels [9]. They have an economical advantage over to the austenitic stainless steels since the austenitic stabilizing element Ni is not needed.

X20 type stainless steel

X20 type of steel is a ferritic/martensitic stainless steel. It is a low carbon stainless steel in which chromium (11 wt.%) is the major alloying element. The composition for the X20 used in this work is given in Paper III. The ferritic/martensitic microstructure results in small steel grains, compared to typical austenitic steel grains.

2.2.2 Austenitic stainless steels

Sufficient addition of certain alloying elements makes it possible to preserve the austenite structure at room temperature. The minimum addition of Cr and Ni required in order to form austenite at room temperature is approximately 18 wt.% Cr and 8 wt.% Ni [9]. If the Cr content is changed, to a lower or a higher amount, more Ni is needed, see the Schaeffer diagram in Fig. 2.4. The austenitic steels are widely used in domestic and industrial applications. One of their most important characteristics is the high corrosion resistance.

304L type stainless steel

The most common austenitic stainless steels are the so-called 18/8 steels containing around 18 wt.% Cr and 8 wt.% Ni. Thus, they have the lowest amount of Ni content with a fully austenitic structure. The stainless steel type 304L, composition given in Paper VI, belongs to this type of stainless steels.

353MA type stainless steel

The 353MA type stainless steel is an alloy designed to withstand oxidation at elevated temperatures. It contains, like other high-alloyed Fe-Cr-Ni stainless steels designed for high temperature applications, a high concentration of Cr (25 wt.%) and Ni (35

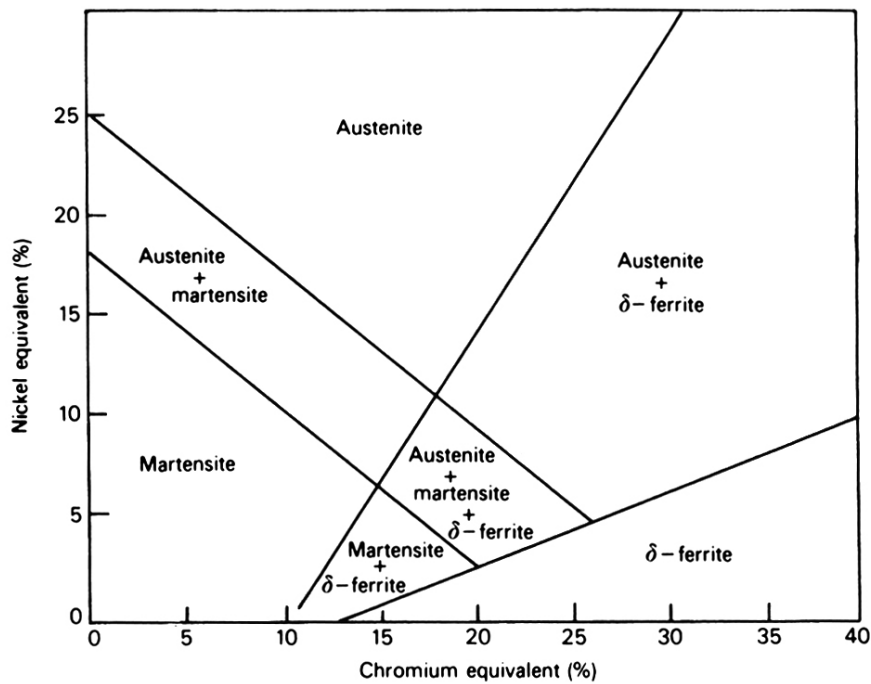


Figure 2.4: Schaeffer diagram showing the effect of alloying elements on the basic structure of Cr-Ni stainless steels [9].

wt. %). One thing that separates alloy 353MA from other conventional stainless steels is the additions of more Si and the reactive element (RE) Ce. It is suggested that Si can, if added in enough concentrations, form a diffusion barrier by forming a dense SiO_2 layer [10-12]. The effect of small additions of RE is known as the “reactive element effect”. It has been identified that the presence of REs in the steel can decrease the oxidation rate [13-16]. However, the exact role the RE plays is not fully understood. The composition of the 353MA steel is given in Paper IV and V.

Chapter 3

Oxidation mechanisms

3

The oxidation mechanisms of alloys used in high temperature applications are generally complex. This is since modern alloys contain a number of elements, as described in the previous chapter, and that many application environments are complex. It is therefore an advantage to work with simplified systems in order to build knowledge about the oxidation process in steps. This can be achieved by studying the impact of a simple environment, *e.g.* oxygen with water vapour, or by using pure metals or model alloys.

The work carried out within the scope of this thesis has been performed on iron and different stainless steels. The focus of this chapter will therefore be on the oxides formed on these metals and alloys. General backgrounds of the different mechanisms treated in this thesis, *i.e.* the effect of water vapour, sulphur dioxide and KCl(s) additions, are also included in this chapter.

3.1 General

Oxidation is a natural reaction for a clean metal surface in contact with oxygen. The driving force is to lower the total energy of the system by forming an oxide. At high temperatures the most common oxides are the solid oxides, which can form both amorphous and crystalline structures. However, some metals form liquid or even gaseous oxides. The formation of a solid metal oxide can schematically be written as Equation (3.1), where M represents the metal, O the oxygen and a, b are integers.



After the first thin oxide film has formed on the metal surface the reaction can only continue by diffusion through the oxide film. The oxide growth is therefore generally dependent on solid-state diffusion. The classical Wagner treatment of oxidation

rates describes this phenomenon. Diffusion of the reacting atoms, ions or electrons through a dense single-phase oxide layer is the rate-determining step for the oxide growth rate [17]. Temperature is one of the most important factors for the diffusion rate and thereby growth rate, since the solid-state diffusion rate increases rapidly with temperature [18-20].

The solid-state diffusion rate is dependent on how dense the oxide scale is. The crystal structure of the oxide scale and the number of lattice defects are therefore important for the oxide growth rate. If the oxide scale is dense it will form a protective slow growing oxide scale. The diffusion rate at moderate temperatures, *e.g.* 500 °C to 900 °C for Fe-Cr alloys, is in addition very dependent on the density of oxide grain boundaries if the oxide is crystalline. This since the more open structures of the grain boundaries offer faster diffusion channels than the lattice in this temperature range. The phenomenon is called “short-circuit” diffusion and has a lower impact at higher temperatures [19]. In some cases microcracks can be formed in the oxide scale or spallation of the oxide scale can occur. These types of phenomenon will then increase the oxidation rate by opening fast channels between the two reactants.

The oxides can be ionic or covalent, but are usually a combination of both. Ionic oxides are often non-stoichiometric, which affects the physical properties of the oxide. Different oxides can generally be classified as either n- or p-type semiconductors. This classification makes it possible to predict the electrical properties of the oxide scale and thereby better understand the diffusion mechanisms through the oxide. By knowing the defect structure in the oxide it can be possible to predict which solid-state transport dominates through the oxide scale, metal or oxygen diffusion. A schematic drawing of oxide growth through cation and anion transport is shown in Fig. 3.1 [18]. However, in real oxide scales this is more complex. Especially when working with alloys built up by a number of elements at moderate temperature.

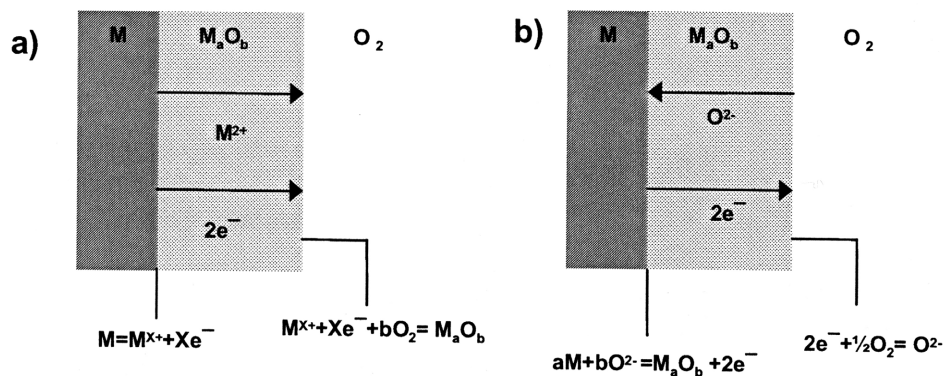


Figure 3.1: A schematic drawing of oxide growth through (a) cation transport and (b) anion transport [18].

3.1.1 Oxidation kinetics

A study of the oxide growth rate gives important information about the oxidation mechanisms. Two methods to measure the oxide growth were used in connection to this work. Weight gain measurements after exposure (series of different exposure times) and thermogravimetric analysis (TGA), where weight gain is measured during the exposure. TGA is performed *in-situ*, which is an advantage when working with high temperatures since the oxide could crack and spall off during the cooling process if the oxide have different thermal expansion coefficient than the metal. The oxide growth analyzed through weight gain is however an average of all the oxide formed on the sample. An *in-situ* environmental scanning electron microscope (ESEM) study of the surface morphology can give additional information about local variations of the oxide growth during the exposure. This since the morphology evolution is imaged in the ESEM during exposure, which in this case is performed within the microscope. This technique was employed to perform *in-situ* exposures and analysis in an ESEM, see Paper II. The ESEM technique is described in section 4.1.1.

The oxide growth can ideally mainly be divided into three categories: logarithmic ($x \propto \log(t)$), parabolic ($x^2 \propto t$) and linear ($x \propto t$), where x represents weight gain and t time, see Fig. 3.2 [19]. The logarithmic growth is initially very rapid and decreases then to a very low value. It is common for metals at lower temperatures, typically below 300 °C. The rate-limiting step is known to be tunneling of electrons through the oxide scale. The classical Wagner mechanism, *i.e.* the rate-limiting step is diffusion of electrons or ions through the scale, results in a parabolic growth rate. A linear reaction rate is constant in time independent on the scale thickness. One example of linear growth rate is when the surface reaction is the rate-limiting step. However, for most alloys the growth rate is a combination of the ideal cases.

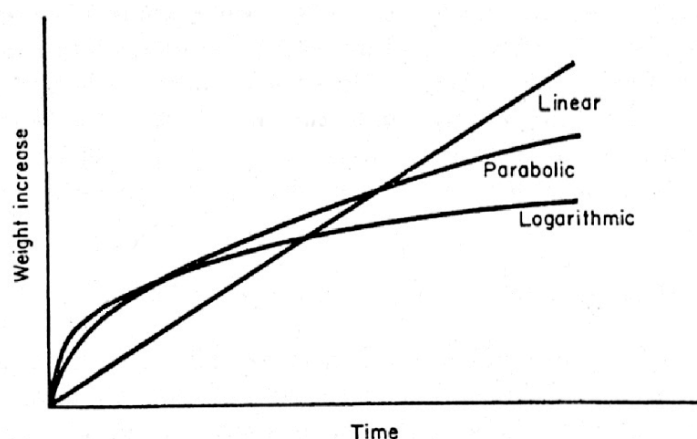


Figure 3.2: The oxidation growth can ideally be divided into the following classes: logarithmic ($x \propto \log(t)$), parabolic ($x^2 \propto t$) and linear ($x \propto t$), where x represents weight gain and t time.

The oxide growth could also display another type of behavior called “breakaway oxidation”. At a certain time the growth increases rapidly because the oxide scale has lost its protective properties, see Fig. 3.3. This behavior can for example be caused by spallation of the oxide scale causing a faster oxidation after some time. Another mechanism is known to cause breakaway oxidation of stainless steels. This can for example be observed for the stainless steel 304L in a high temperature environment containing water vapour [3, 4]. Water vapour reacts with Cr in the oxide and forms a product, probably $\text{CrO}_2(\text{OH})_2$ [21], in the gas phase. This phenomenon decreases the Cr content in the base oxide, *i.e.* the thin protective scale, if the evaporation exceeds the supply of Cr from the steel. The protective Cr rich scale is then transformed to an Fe rich non-protective scale. Since diffusion is slower in the steel bulk than along steel grain boundaries the Cr content in the oxide scale on the middle of the steel grains will decrease faster than on top of steel grain boundaries. This is the reason why breakaway oxidation appears first on the middle of the steel grains and a faster growing oxide forms there. The surface morphology where thicker oxide scales cover steel grains and thinner oxide scales cover steel grain boundaries shows this. The thicker oxide scale can be divided into an outward growing part the (“island”) and an inward growing part the (“crater”), see Fig. 3.4 [4].

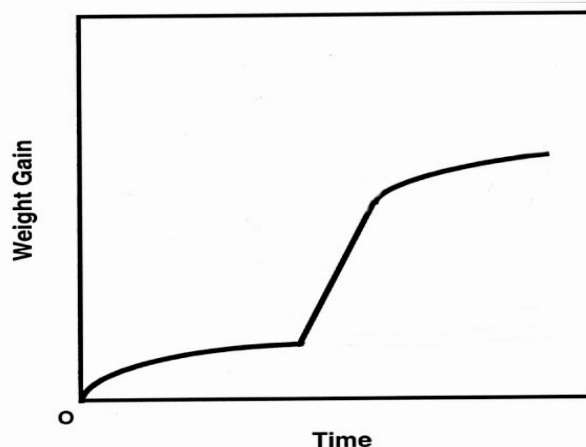


Figure 3.3: Breakaway oxidation behaviour. At a certain time the growth rate increases rapidly because the oxide scale has lost its protective properties. After long time the oxide scale is very thick and the weight gain slows down again.

3.2 Oxides

In order to understand the oxidation behavior of an alloy it is important to understand the properties of the elements with highest affinity for oxygen in the alloy, *i.e.* the elements that will form the oxide. These elements will form the oxide scale either as a solid solution or as different layers. The alloys in this project can mainly form three types of oxide structures. They are rock salt, spinel and corundum structures, see Fig. 3.5. In the following sections the properties of the most important oxides for the materials investigated in this thesis will be described.

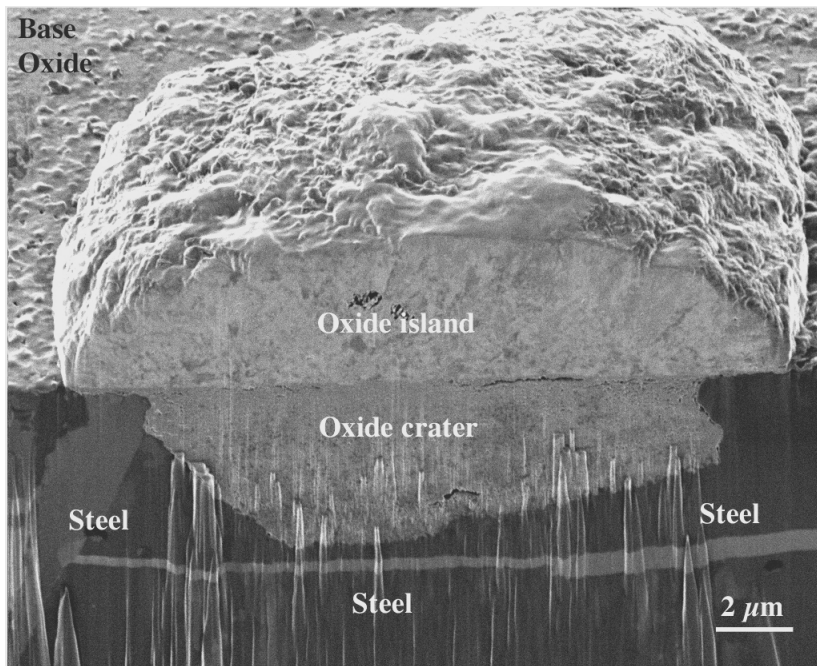


Figure 3.4: An example of breakaway oxidation showing a FIB milled cross-section of an oxide “island” and “crater” formed on a steel grain on 304L stainless steel exposed to oxygen and water vapour [4].

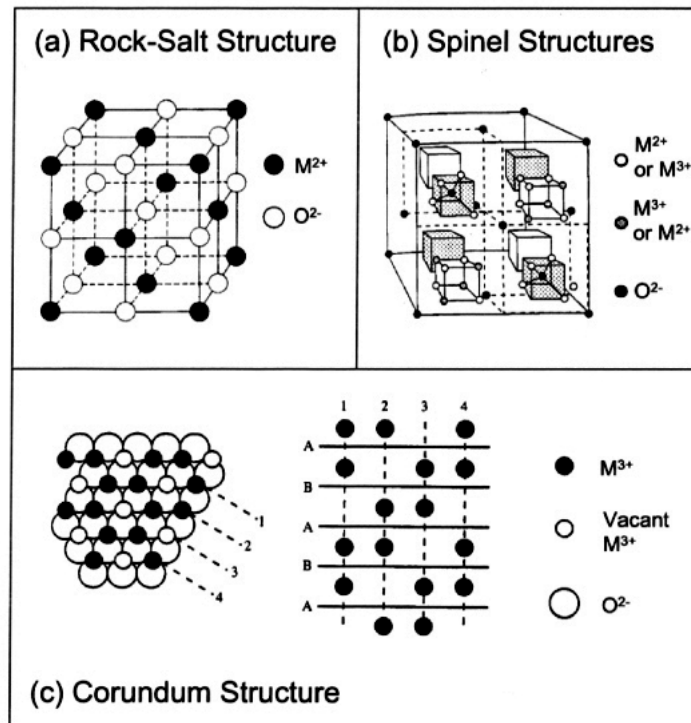


Figure 3.5: Three common metal oxide crystal structures: (a) rock-salt structure, (b) spinel structure, (c) corundum structure [3].

3.2.1 Iron oxide

There are three different types of iron oxides, wüstite (FeO), magnetite (Fe_3O_4) and hematite (Fe_2O_3) [19]. The oxides form a layered scale at high temperatures, *i.e.* wüstite closest to the metal (above 570°C), magnetite in the middle and hematite as the outer layer. This is because wüstite forms at the lowest partial pressure of oxygen and hematite at the highest. Wüstite is known to be the fastest growing iron oxide due to the great mobility of defects [19]. It has a rock salt structure, see Fig. 3.5a, and is classified as a p-type oxide. The phase diagram for Fe-O shows that wüstite is not stable below 570°C , see Fig. 3.6. Magnetite has an inverse spinel structure and contains both Fe^{3+} and Fe^{2+} ions in the structure. It is classified as an n-type oxide. Hematite has a corundum structure, see Fig. 3.5c, and it is also classified as an n-type oxide [19].

The growth of iron oxide above 570°C is generally dominated by the growth of wüstite since the transport of ions and electrons through this layer is fast because wüstite is non-stoichiometric. Magnetite typically forms a thicker layer than hematite. The different diffusion steps and interfacial reactions during growth of a layered iron oxide are shown in Fig. 3.7 [18].

Sample preparation is believed to be important for the oxide growth kinetics and for the oxide scale adherence [22]. The thickness ratios of the hematite and magnetite

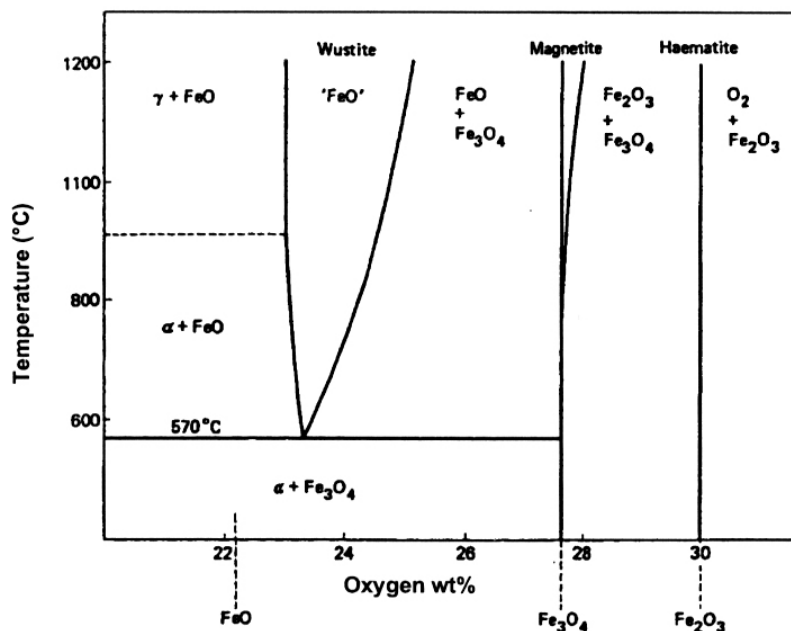


Figure 3.6: The iron-oxygen phase diagram [18].

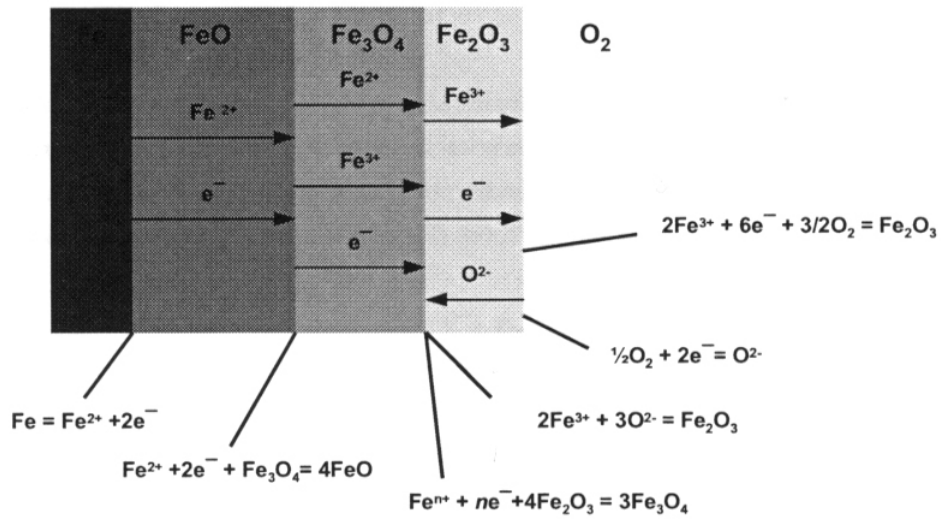


Figure 3.7: The different diffusion steps and interfacial reactions of the oxidation of iron above 570°C [18].

layers formed on mechanically polished samples have been reported to be between 1:10 and 1:20 [22]. Iron oxide has in addition been reported to form a three-layered scale below 570 °C [22] (Paper I and II). An example of this can be seen on iron exposed for 24 hours at 500 °C in dry oxygen, see Fig. 3.8 (Paper I). The inner two layers are both magnetite formed below a thinner hematite layer.

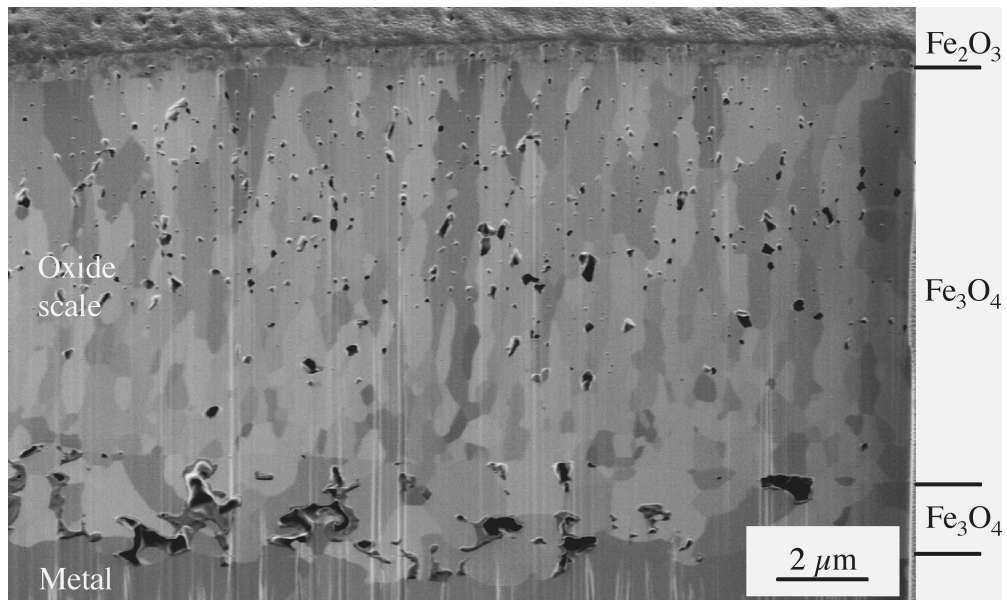


Figure 3.8: An example of a three-layered iron oxide scale formed below 570 °C. The sample has been exposed for 24 hours at 500 °C in dry oxygen (Paper I).

3.2.2 Chromium oxide

Oxidation of chromium at high temperature produces only one stable oxide. Chromium oxide, eskolaite (Cr_2O_3), forms a very dense and thereby slow growing oxide in a wide temperature range [19]. It has a corundum structure, see Fig. 3.5c, and is classified as a p-type oxide. Eskolaite is generally believed to grow by cation diffusion in combination with some anion diffusion, mainly along grain boundaries [19].

The use of Cr to form a protective oxide is limited by $\text{CrO}_3(\text{g})$ evaporation at temperatures above 1000 °C [19]. It has in addition been shown that Cr evaporates from the oxide in a lower temperature range, 500 °C to 900 °C, if there is water vapour in the environment [3, 4, 23]. The product has been suggested to be $\text{CrO}_2(\text{OH})_2(\text{g})$ [21]. This phenomenon will be described in more detail in section 3.4.2.

3.2.3 Silicon oxide

Silicon oxide, silica (SiO_2), can form a dense, often amorphous oxide. Si has lower affinity for oxygen than Fe and Cr and will therefore form silica as an inner oxide layer, between the metal and the Cr-Fe oxide scale. Si is added to some stainless steels with the intention to form a dense oxide layer beneath the surface oxide [24, 25].

3.3 Oxidation of stainless steels

The Cr content plays an important role for the oxide's growth rate on stainless steels. At high enough concentrations of Cr, about 10 wt.%, Cr atoms will be selectively oxidized and form a Cr rich slow-growing protective oxide. The amount of Cr in the alloy is therefore very important for the oxidation properties. However, the exact level needed to form the protective oxide scale depends on the environment and the microstructure of the steel.

Eskolaite and hematite both have a corundum structure, see Fig. 3.5c, and can form a solid solution $(\text{Fe,Cr})_2\text{O}_3$, which is stable at high temperatures. The oxide scales on Fe-Cr alloys will be composed of such a solid solution. It is the properties of the $(\text{Fe,Cr})_2\text{O}_3$ solid solution that determine how protective the oxide scale is. This is the reason why it is important to understand how the properties of the oxide scale change when the content of Fe and Cr changes in the solid solution $(\text{Fe,Cr})_2\text{O}_3$. However, it is not clear at what Cr/Fe ratio the oxide loses its protective properties. The lowest observed level of Cr in a thin scale was about 50 wt.% (cations) in this work (Paper VI). The Fe-Cr system can in addition form a spinel oxide structure $(\text{Fe,Cr})_3\text{O}_4$ at lower oxygen partial pressure. This type of oxide is found as the inward growing oxide after breakaway oxidation [4]. An example of the inward growing $(\text{Fe,Cr})_3\text{O}_4$ "oxide crater" can be seen in Fig. 3.4.

Other alloying elements can frequently be found in the oxide scale formed on stainless steels. Two examples are Mn and Ni. Even though the Mn content is generally low in stainless steels it can often be found in the outer part of the oxide scale. Ni can typically be found in spinel phases if the content in the steel is substantial, *e.g.* for the stainless steel 353MA.

3.3.1 Influence of alloy microstructure

The supply of Cr to the oxide scale is very important for high temperature oxidation of Fe-Cr alloys in corrosive environments, *e.g.* O₂/H₂O mixtures, in order to maintain a Cr-rich protective oxide scale. This is the reason why the microstructure of the material below the oxide scale is important for the oxidation behavior. The ferritic/martensitic microstructure of the stainless steel X20, described in section 2.2.1, has small steel grains compared to the typical austenitic microstructure, described in section 2.2.2. This together with the faster diffusion in the less dense ferritic/martensitic structure results in a relatively evenly distributed diffusion of Cr from the steel bulk to the oxide scale compared to austenitic steels. Temperature is very important for this phenomenon since the difference between grain boundary diffusion and bulk diffusion is very temperature dependent. There is a difference between bulk and grain boundary diffusion for these stainless steels at moderate temperatures (500 to 900 °C).

3.4 Previous studies

The influence of three different species in the exposure environment on the oxidation is treated in this thesis. They have all partly been investigated by other researchers previously. In this section a general background will be given regarding these previous studies.

3.4.1 The effect of sulphur dioxide

The effect of sulphur dioxide has been investigated in several studies [26-30]. Most of these investigations have been performed with high concentrations of SO₂ or in many cases with only SO₂ in the gas phase. It is generally believed that a high concentration of SO₂ in the gas phase increases the oxidation rate of metals and alloys. The reason is suggested to be the formation of sulphides in the oxide scale, which increases the ion diffusion rate and therefore the oxidation rate. There are however important applications where the level of sulphur dioxide is low. One example is the combustion gas in a power plant where the level of sulphur dioxide typically is 10-1000 ppm. It is therefore important to investigate the effect of lower levels of SO₂ on the oxidation mechanism of metals and alloys, as in Paper I.

Investigations of the effect of low levels of SO₂ on the oxidation have been performed by Järtnäs *et al.* [2]. The effect of low levels of SO₂ on oxidation of pure iron, Fe-2.25Cr-1Mo and pure Cr were studied. It was concluded that low levels of sulphur

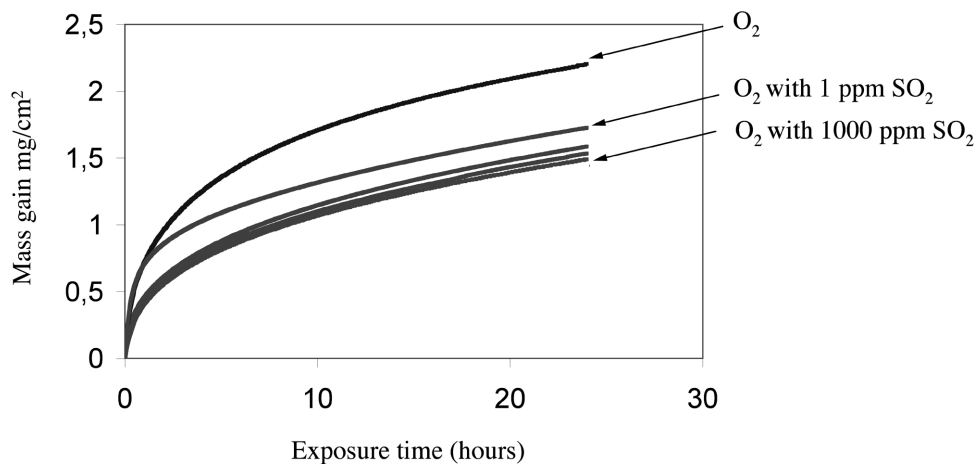


Figure 3.9: Mass gain curves of iron exposed in O_2 and in O_2 with low levels of SO_2 at $500\text{ }^\circ\text{C}$ [2]. The SO_2 levels are 0, 1, 10, 100 and 1000 ppm.

dioxide slow down the oxidation rate up to $650\text{ }^\circ\text{C}$. No effect could be seen over $650\text{ }^\circ\text{C}$. It was suggested that the effect of low levels of sulphur dioxide could be attributed to the formation of a thin layer of sulphate on the surface. In Fig. 3.9 the oxidation kinetics are shown for iron in different O_2/SO_2 mixtures at $500\text{ }^\circ\text{C}$ [2]. This shows that the oxidation kinetics changes if small additions of sulphur dioxide are added to the environment.

3.4.2 The effect of water vapour

The presence of water vapour is known to change the oxidation behaviour of metals and alloys compared to oxidation in dry oxygen. It is generally known to increase the corrosivity of the environment. Researchers have presented several studies treating the water vapour effect on iron and on Fe-Cr(-Ni) steels over the years. However, most of the earlier investigations on the water vapour effect have been carried out at high temperatures, $T > 900\text{ }^\circ\text{C}$, which is typically above the maximum service temperature for the materials investigated in this thesis.

Iron

There are some publications dealing with the effect of water vapour on the oxidation of iron at high temperature [31, 32]. An increased oxidation rate was reported at $950\text{ }^\circ\text{C}$ in the presence of 10% H_2O while no effect was reported at $750\text{ }^\circ\text{C}$ [31]. The increased oxidation rate at $950\text{ }^\circ\text{C}$ was explained by fast transport of oxygen by H_2O or Fe by $Fe(OH)_2(g)$ through pores by an oxidation/reduction mechanisms. However, the influence of water vapour on the oxidation of iron is not fully understood [19].

Fe-Cr alloys

Generally, it is believed that a higher Cr content is needed in Fe-Cr alloys if water vapour is present to form a protective scale than in dry oxidizing environments [19, 33]. Several explanations have been suggested for the corrosivity of O_2/H_2O mixtures [3, 4, 23, 33-37]. The material transport mechanisms have been reported to change, normally increase, in the presence of water vapour [34]. Hydrogen has been reported to become incorporated into the oxide scale, changing the defect-dependent properties [36, 37].

Exposure to O_2/H_2O mixtures in the temperature range 500 to 900 °C, have been reported to result in chromium evaporation. According to Ebbinghaus the most probable vaporising species is $CrO_2(OH)_2$ in this temperature range [21]. Both austenitic and ferritic stainless steel have been investigated in the presence of water vapour in this temperature range [3, 4, 23]. Asteman *et al.* investigated the water vapour effect on the austenitic stainless steel 304L [3]. In Fig. 3.10 the oxidation kinetics are shown for 304L in dry and wet oxygen at 600 °C [3]. This shows that the oxidation kinetics change in the presence of water vapour, causing breakaway oxidation. Tang *et al.*, on the other hand, performed a microstructural investigation of 304L exposed in dry and wet oxygen [4]. Breakdown of the protective oxide scale was shown to cause the formation of an outward growing and an inward growing oxide, see Fig. 3.4. One important conclusion from these investigations was that Cr evaporation could lead to Cr depletion of the protective oxide resulting in the formation of a poorly protective Fe-rich oxide, causing an increased oxidation rate. The ability of an alloy to endure Cr vaporisation without losing the protective properties of the oxide is expected to depend on the rate of supply of Cr from the alloy to the oxide scale.

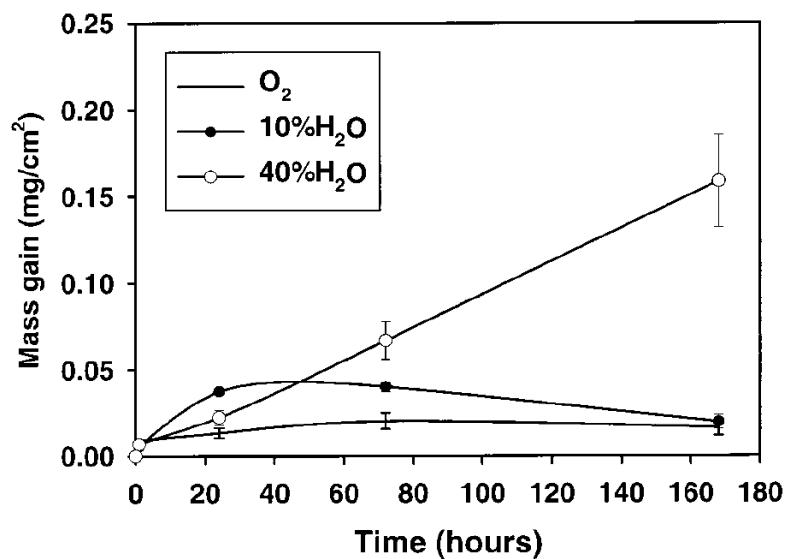


Figure 3.10: 304L oxidized isothermally in dry O_2 , $O_2 + 10\% H_2O$ and $O_2 + 40\% H_2O$ at 600 °C [3].

3.4.3 The effect of KCl(s)

The presence of alkali chlorides is known to increase the corrosion of stainless steels. An example of this can be seen in Fig. 3.11 where the oxidation kinetics for 304L, with and without small KCl(s) additions, at 600 °C is shown [38]. The oxidation rate is much higher in the presence of KCl(s). The corrosive effect of alkali chlorides has previously been investigated [5-8, 39]. However, alkali chlorides have generally been regarded as a way to form molecular chlorine. The molecular chlorine has been suggested to increase the corrosion rate by the formation of volatile transition metal chlorides at the scale/metal interface, the so-called “active oxidation” mechanism. This mechanism was used to explain the increased corrosion rate of iron in Cl₂ containing atmospheres [40]. Another explanation for the corrosivity of alkali chlorides based on the formation of eutectic melts of NaCl-Na₂CrO₄ have been proposed [41]. In addition it has recently been proposed that KCl destroys the protective oxide in a similar way as water vapour [23, 38, 42]. Instead of forming gaseous CrO₂(OH)₂, as in the presence of water vapour, chromium was suggested to be depleted in the base oxide by the formation of K₂CrO₄ particles.

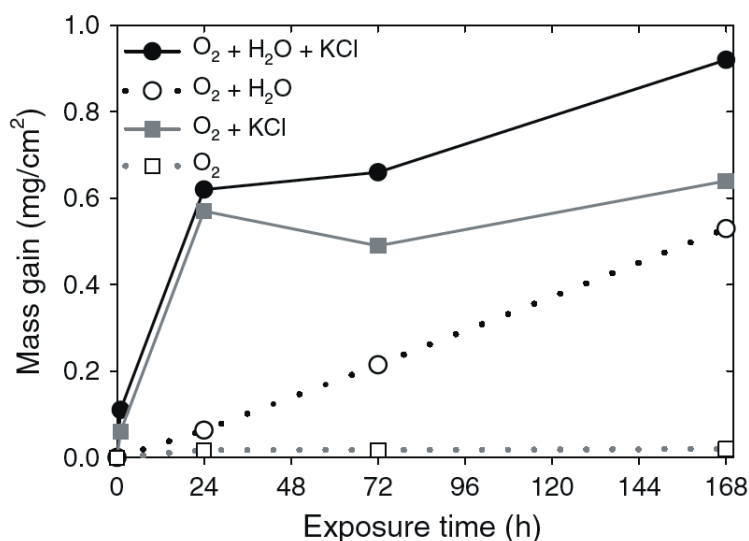


Figure 3.11: 304L oxidized isothermally in dry O₂ and O₂ + 40% H₂O at 600 °C with and without KCl(s) [38].

Chapter 4

Experimental techniques

4

The experimental work in this thesis, *i.e.* the microstructural investigations, has been performed by analytical electron and ion microscopy. The microstructure has then been linked to the exposure conditions in order to gain further understanding about the oxidation mechanisms. Several different instruments have been used: a scanning electron microscope (SEM) with an energy dispersive X-ray (EDX) detector and an electron backscattering system (EBSD), an environmental SEM (ESEM) with a heating stage for *in-situ* exposures and analysis, a focused ion beam (FIB) workstation, a FIB/SEM workstation and a transmission electron microscope (TEM) with an EDX detector. Furnace exposures and complementary analysis of the samples, *e.g.* X-ray diffraction (XRD), were performed by collaborators at the Department of Chemical and Biological Engineering at Chalmers University of Technology.

Several factors must be taken into account when selecting the most suitable technique, *e.g.* spatial resolution and sample preparation requirements. In this work the FIB workstation was used to investigate the surface morphology of the oxide, to mill cross-sections and to prepare electron transparent regions for TEM investigations. The FIB/SEM workstation was used to prepare electron transparent cross-sections for TEM investigations by the *in-situ* liftout technique when the standard FIB technique was inadequate to produce TEM samples, *e.g.* for thin oxides or samples containing water-soluble species. The SEM was used to investigate the surface morphology and to determine the chemical composition of the oxides through EDX mapping, linescans and quantification. It was in addition used to image metal grains prior to exposure by channeling contrast of forward scattered electrons (FSE) and the ESEM was used for *in-situ* exposures and analysis. In order to investigate details in the oxide with higher spatial resolution the TEM was used.

4.1 Exposures

For some of the samples used in this work the exposures were performed *in-situ* in the ESEM. This made it possible to study the oxide growth at temperature. In addition samples exposed in furnaces were received from the Department of Chemical and Biological Engineering at Chalmers University of Technology. Therefore, only a short description will be given of the sample preparation prior to the furnace exposures and the experimental set-up during those exposures [2, 23].

4.1.1 ESEM *in-situ* exposures

An ESEM can be operated with a low vacuum in the sample chamber. The low vacuum can be used in combination with a heating stage in order to study solid/gas reactions, *e.g.* high temperature oxidation, *in-situ*. A detailed description of the ESEM is given in section 4.3. A heating stage typically consists of a furnace, a thermocouple and a water-cooling system. Fig. 4.1 shows an image of the ESEM sample chamber prepared for high temperature exposure and analysis. The sample is positioned in a small sample holder on the heating stage beneath the special heat and light insensitive secondary electron detector used for imaging at high temperature [Fig. 4.1]. The temperature is ramped to the required temperature with a maximum ramping speed of 50 °C/minute. Fig. 4.2 shows an example of how the *in-situ* technique can be used to study high temperature oxidation of pure iron. The growth of the iron oxide is imaged *in-situ* at 500 °C after different exposure times. The formation of iron whiskers on different regions can be imaged during the exposure, which gives unique information about the initial distribution and growth.

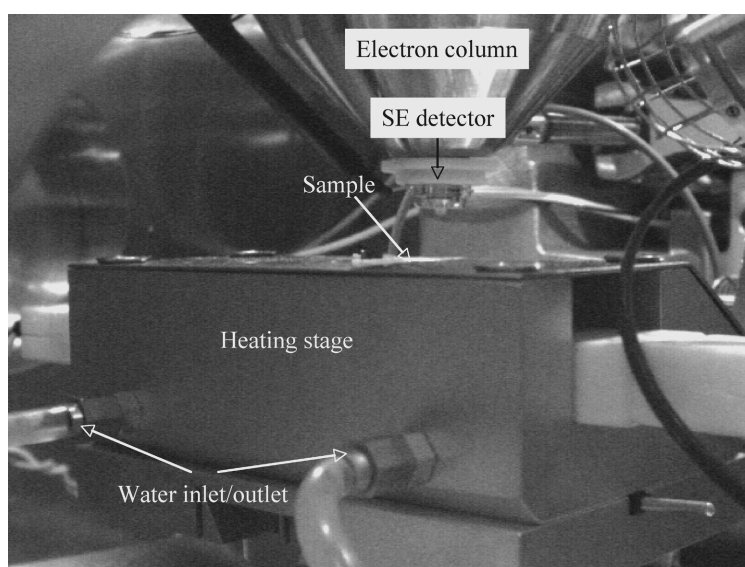


Figure 4.1: The ESEM sample chamber prepared for high temperature *in-situ* exposure and analysis.

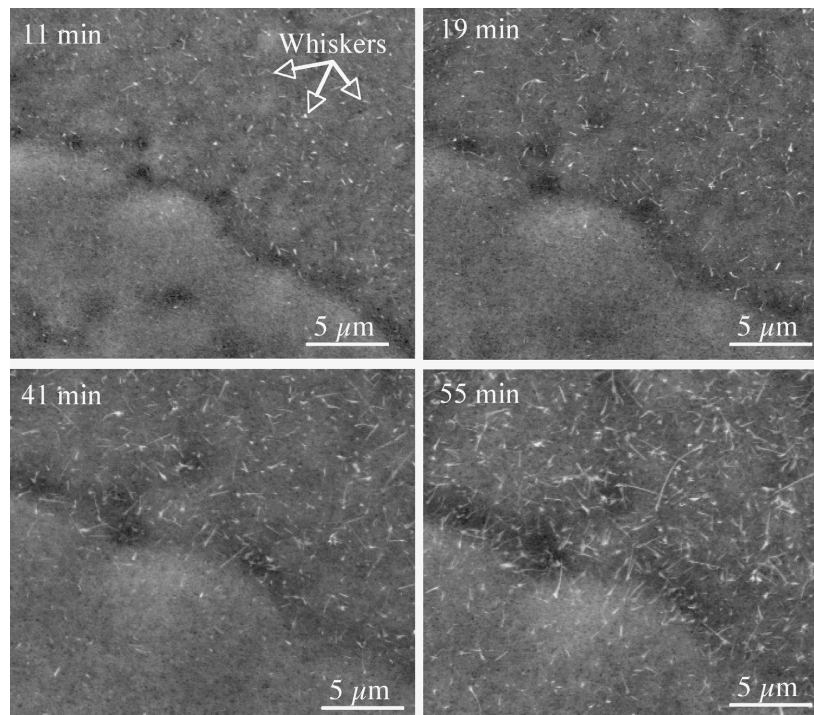


Figure 4.2: *The growth of the iron oxide on iron imaged in-situ at 500 °C (different exposure times). The whisker growth on different regions can be followed.*

4.1.2 Isothermal furnace exposures

First 15x15x2 mm coupons were cut and polished using 1000-mesh SiC paper. Then the coupons were polished with diamond paste, the finishing polish was done with 1 μm paste. The samples were then cleaned with ethanol using ultrasonic agitation and stored in a desiccator before exposure. Three samples were exposed at the same time in the furnace. The temperature, flow velocity, water vapour/sulphur dioxide concentration and exposure time could be varied. After the exposures all samples were removed and allowed to cool to room temperature in dry air. Mass changes of the samples were recorded after the exposure by the use of a five or six decimal balance. The weight gains correspond to the difference between the weight of the sample after and before the exposure in the furnace.

4.1.3 Thermogravimetric analysis (TGA)

In order to be able to record the mass change of the sample continuously during the exposure a SETARAM TAG24S 16 thermogravimetric analysis system (TGA) was used. It is equipped with a balance capable of recording mass changes as small as 0.2 μg . Metal coupons with dimensions 10x8x2 mm³ were used. A 1.5 mm hole was drilled for suspending the samples, which then were prepared in the same way as the samples used for furnace exposures. The thermobalance is equipped with a double symmetrical furnace. A piece of sintered Al₂O₃, with the same dimensions as the

sample, was used as a counterweight and a silica glass wire suspended the sample during the exposure. After the exposure all samples were removed and allowed to cool to room temperature in dry air.

4.2 Scanning electron microscope (SEM)

A conventional SEM has a high spatial resolution, good depth of focus and the possibility to perform chemical analysis of the sample if the microscope is equipped with an EDX detector. For this work a Leo Ultra 55 SEM equipped with a field emission gun (FEG), an Oxford Inca EDX system and a HKL (Channel 5 software) EBSD system was used.

4.2.1 The design of the SEM

A schematic drawing of a standard SEM is shown in Fig. 4.3. The electrons are emitted from an electron source and are then accelerated in the electron gun. There are several different types of electron sources available. The three most common are the thermoionic W and LaB₆ together with the FEG. The quality of the source is important since it will influence the resolution. The electrons pass through a system of magnetic lenses and apertures before reaching the sample, see Fig. 4.3. The condenser lens controls the spot size while the objective lens controls the focus. The main functions of the lenses and apertures are to focus and make the probe size as small as possible on the sample surface with as high current of electrons as possible.

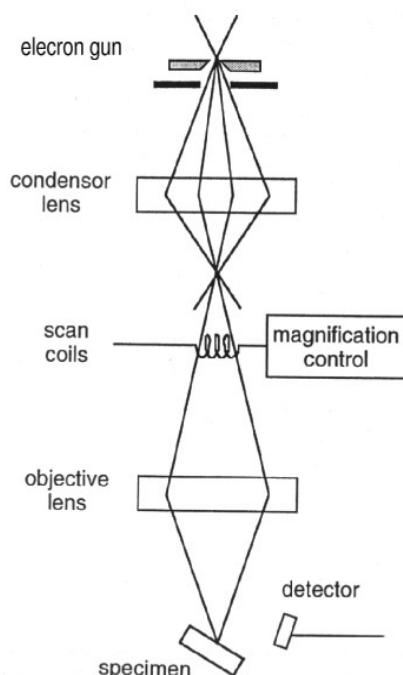


Figure 4.3: A schematic drawing of an SEM.

It is important that there is a high vacuum in the column and in the sample chamber. Otherwise electrons would interact with gas molecules and thereby be impossible to focus on the sample. Several detectors can be placed in the sample chamber. The three most commonly used are secondary electron detectors, backscattered electron detectors and EDX detectors.

4.2.2 Contrast mechanisms and imaging modes

As the electron beam is scanned in a raster across the specimen's surface the detected signal is transformed and shown on the computer screen. The magnification is given by the ratio between the length displayed on the computer screen and the scanned length on the specimen.

Important signals emitted from the sample generated by the incoming primary electrons are secondary electrons (SEs), backscattered electrons (BSEs) and X-ray photons. The different kind of signals can escape from different depths in the sample, *i.e.* have different spatial resolution [43], see Fig. 4.4.

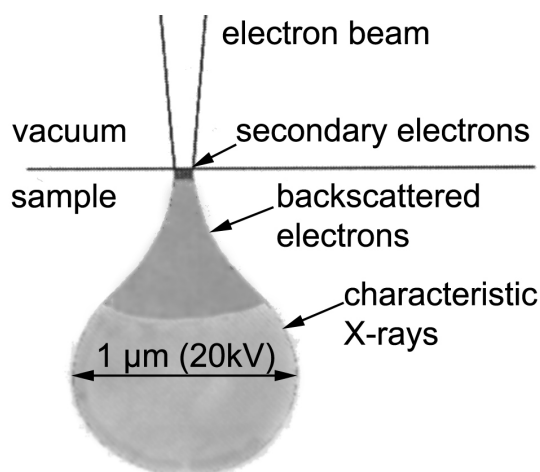


Figure 4.4: *The interaction volume from which the different signals are generated in the SEM. Secondary electrons can only escape from a volume close to the surface while backscattered electrons and X-rays can escape from much larger volumes. The size of the interaction volume is strongly dependent on the acceleration voltage, but is 1 μm at 20 kV.*

Secondary electrons (SEs)/Backscattered electrons (BSEs)

Electrons emitted from the sample are divided into two different categories in the SEM: SEs have low energy (<50 eV) and can only escape from a region close to the surface. The SEs therefore give the best resolution, approximately 1-5 nm, and are often used to view topographical contrast, which is created because of the “edge effect”. Edges of surface features will emit more electrons than a flat surface, which

creates the contrast. BSEs have higher energy and thereby a larger escape depth, *i.e.* lower spatial resolution. The amount of BSEs depends on the composition and the sample geometry. A material with higher atomic number (Z) gives more BSEs.

Energy dispersive X-ray (EDX)

If a high-energy electron transfers enough energy to release an inner shell electron, thereby removing it from the atom, the atom can relax by emitting a photon, see Fig. 4.5. These types of photons have a specific energy coupled to the atom they were released from, which makes it possible to perform chemical analysis. The X-rays can escape from an even deeper region than the BSEs, see Fig. 4.4, which explains why the EDX analysis has the lowest resolution, about $1\ \mu\text{m}$ at an acceleration voltage of 20 kV [43].

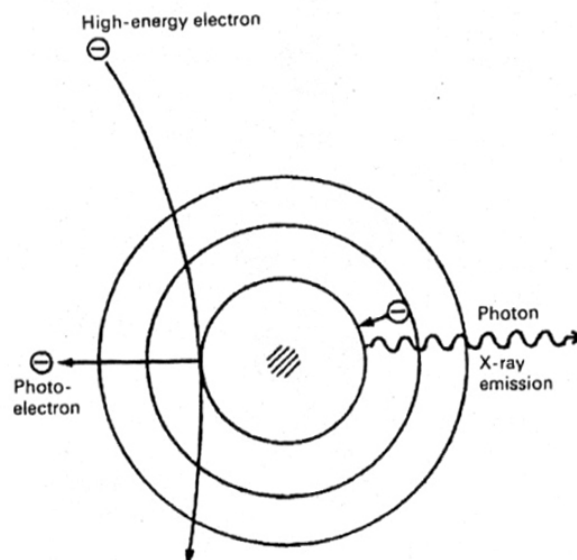


Figure 4.5: The process leading to characteristic X-ray emission in the SEM.

The accuracy of quantitative EDX analysis depends on several factors. Light elements release low energy photons and are therefore difficult to quantify with high accuracy. Even for heavier elements several factors must be compensated for to be able to perform an accurate quantification. The “ZAF correction” compensates for three factors that could affect the accuracy. The atomic number affects the electron scattering (Z factor), X-rays can be absorbed within the specimen (A factor) and the fluorescence effect is caused by photons from one type of atoms exciting another type of atoms (F factor). Even though these corrections are performed the results from quantitative EDX analysis have to be handled with care. In order to validate the accuracy of the quantitative analysis during this work quantification was regularly performed on parts on the sample with known composition, *e.g.* the unoxidised metal far below the oxide scale.

By lowering the acceleration voltage in the SEM it is possible to increase the spatial resolution for the BSE and the EDX analysis. The interaction volume is strongly dependent on the acceleration voltage, lower acceleration voltage gives a smaller interaction volume and thereby a better resolution [43]. However, the acceleration voltage must be high enough to excite all the elements in the sample in order to be able to perform EDX. The lowest possible accelerating voltage is not always limited by the formation of K peaks, which are commonly used for EDX analysis. When using L peaks for analysis it is however important to use the highest possible energy resolution in the spectra to avoid overlaps between peaks from different elements. The quantitative analysis will have a lower accuracy when using L peaks instead of K peaks.

Electron channelling contrast

If the sample is crystalline the incoming electrons will penetrate different depths of the sample depending on the orientation of the lattice. When the planes are ordered so that the incoming electrons encounter a low density of atoms a fraction of the primary electrons will penetrate deeper into the crystal before being scattered. This results in less BSEs. The effect is more apparent when the sample is tilted about 70° [43]. This phenomenon can be used for imaging with forward scattered electrons (FSE) and for EBSD. The forward scattered electron detector can be used in order to image for example different metal grains, *i.e.* different crystal orientations give different amount of forward scattered electrons. An example of this is shown in Fig. 4.6. It is a polished polycrystalline iron sample where the different metal grains can be distinguished in the FSE image.

The forward scattered electrons and the channeling effect can be used in order to determine the crystal structure (EBSD). This since the forward scattered electrons will interact with the lattice creating a pattern of parallel lines “kikuchi lines”. These lines can then be recorded by a CCD camera and processed in order to identify the crystal structure.

4.3 Environmental scanning electron microscope (ESEM)

For this work two different ESEMs were used: an ESEM Electro Scan 2020 with a Link Isis EDX system and an FEI Quanta 200 ESEM FEG equipped with an Oxford Inca EDX system. The FEI Quanta 200 ESEM FEG is also equipped with an external temperature control unit for heating experiments together with a heating stage. Both instruments were used for imaging and EDX analysis while only the FEI Quanta 200 FEG ESEM was used for *in-situ* exposure and analysis.

4.3.1 The design of the ESEM

The special feature that separates the ESEM from a conventional SEM is that a higher pressure can be used in the sample chamber. This is possible since apertures are positioned between the column and the sample chamber in order to maintain the

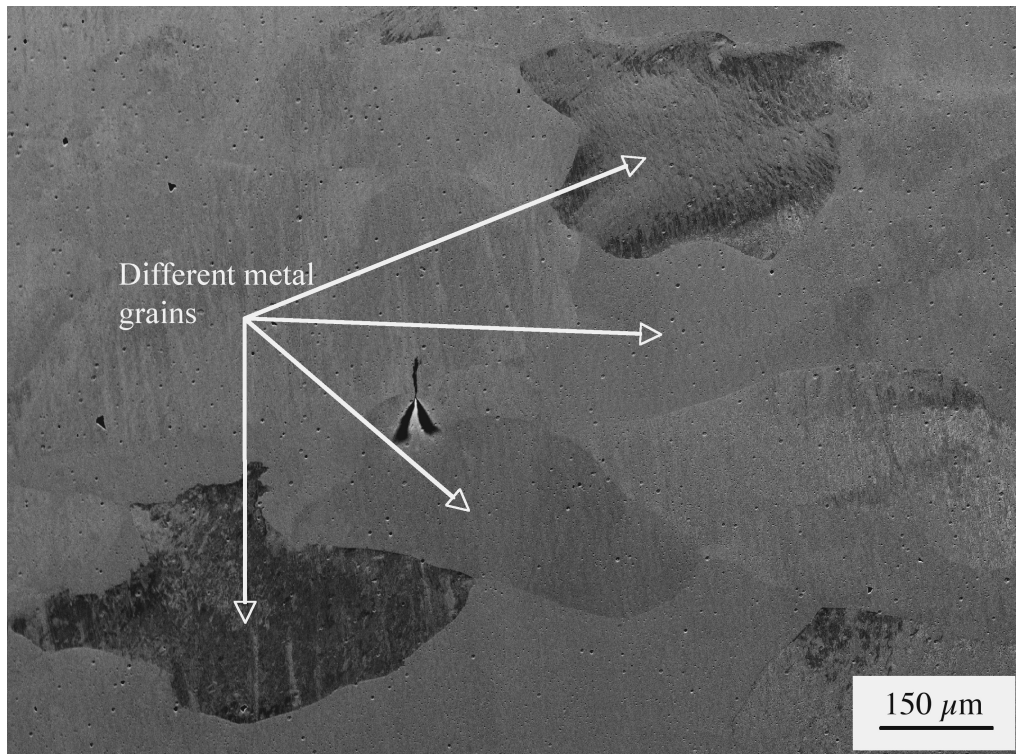


Figure 4.6: A polished polycrystalline iron sample imaged in the SEM with the forward scattered electron detector at 30 kV. The different metal grains can be distinguished in this FSE image.

required high vacuum in the electron column. The apertures let the electron beam through but make it possible to have different pressures in the column and the sample chamber. The pressure in the ESEM sample chamber can therefore be higher than in the SEM, typically up to 20 Torr [43]. It is nevertheless important that the distance the electron beam travels in the sample chamber is kept to a minimum in order to minimize scattering of the primary electron beam. The problem with charging samples is solved in the ESEM by the fact that some of the secondary electrons ionize the gas molecules present in the sample chamber. The positive ions will then neutralize the charge on the sample surface, while the electrons that are created during the ionization process will result in signal amplification.

4.4 Focused ion beam (FIB) workstation

A FIB workstation can be used both as a microscope and as a precision ion-miller. It is in addition possible to insert gas into the sample chamber either to deposit protective coatings or to use as an *in-situ* chemical etch. The drawback is that the specimen surface always will be affected by the ions even when using low current and low magnification in imaging mode. The resolution of modern FIB workstations (~5 nm) is comparable with the resolution of an SEM and the image is created by the same principle as in the SEM with the difference that ions instead of electrons are

accelerated towards the sample. For the work connected to this thesis a FEI 200 THP Thin-film Head Processing FIB with “xp” milling software was used.

4.4.1 Design of the FIB workstation

The main features of the FIB are the same as in the SEM. The ion source, from which the ions are emitted, is important and affects the final resolution of the ion beam. Today many of the modern FIB workstations use a liquid gallium ion source, *e.g.* the FEI 200 THP workstation. The ions pass through several electrostatic lenses. The function of the lenses is to focus the ion beam onto the sample. For the same reason as for the SEM it is important that the ion column and sample chamber are in high vacuum. In the sample chamber there are a secondary electron detector and a needle for injecting different gases close to the sample.

4.4.2 Contrast mechanisms

In the FIB workstation used in this project, only an SE detector was used for imaging. When the ions hit the sample surface ions, X-rays and SEs are emitted. The SE detector collects the secondary electrons and that signal forms an image on the computer screen in the same way as in the SEM. The number of secondary electrons emitted from the sample depends on the ion current, acceleration voltage, the composition and the surface topography. The topographical contrast is formed by the same “edge effect” as in the SEM. In addition the atomic number and the conductivity can affect the number of secondary electrons emitted from the surface. Another useful contrast mechanism is the grain orientation contrast. If the material is polycrystalline and has a smooth surface it is possible to detect different grains due to the interaction of the ions with the crystals. The orientation of the crystals affect the number of secondary electrons that will escape, which makes grains with different orientation appear with different contrast, as with FSEs. In Fig. 4.7 an example of this phenomenon is shown. It is a FIB image of an ion-milled cross-section of iron oxide. The different oxide grains are easy to detect in the FIB image because of the grain orientation contrast.

In the FIB workstation it is possible to tilt the sample so that the ion-milled cross-sections can be imaged directly in the FIB. This function is used together with the crystallographic contrast to image the oxide scales and the subjacent metal. The actual thickness of the oxide scales has to be calculated by using Equation (4.1), because of the tilt. T is the actual thickness, α is the tilt angle and T_0 the observed thickness in the FIB image, see Fig. 4.7.

$$T = T_0 / \sin\alpha \quad (4.1)$$

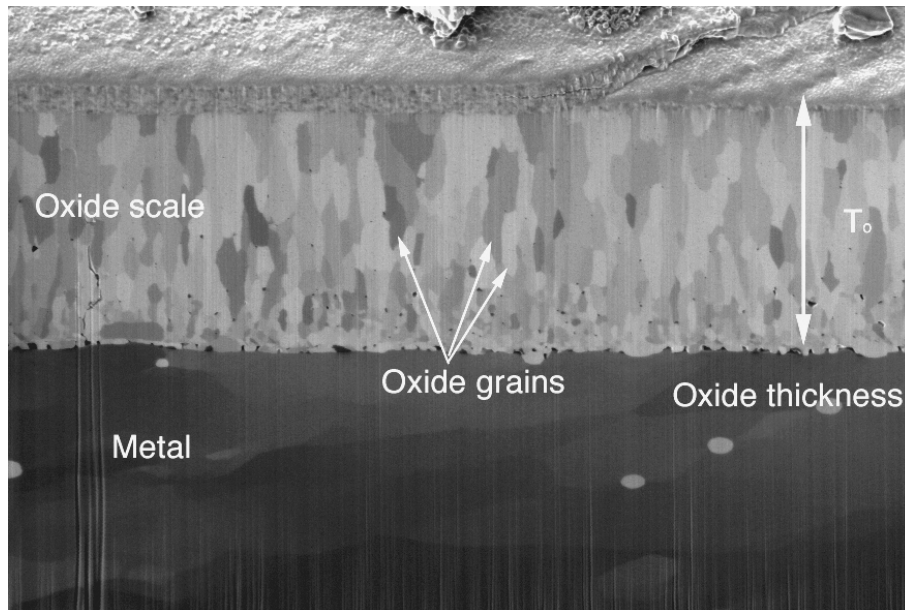


Figure 4.7: A FIB image showing iron oxide in cross-section. The different oxide grains are possible to detect because of the grain orientation contrast in the FIB.

4.4.3 FIB as a milling tool

By selecting a high ion current and focus the scan on a limited area it is possible to use the FIB as a milling tool. The high current of ions will sputter away material. It is though important to notice that a high ion current will result in a lower milling accuracy since the distribution of the ions is wider for higher currents, *i.e.* the beam tail is wider. Another drawback with high ion current is it may generate more redeposition. It is therefore important to lower the ion current during the milling procedure if higher accuracy is required. The ion milling is therefore started with a high ion current, for more rapid coarse milling; the ion current is then lowered when the demand for accuracy increases.

4.4.4 Gas injection system

In the FIB workstation it is possible to inject gas into the sample chamber through a needle. The needle can, with high accuracy, be directed to inject gas over a specific region on the sample. This feature makes it possible to deposit a coating on a selected part of the sample surface or to inject a gas that will speed up the milling procedure, which then works like a chemical etch together with the ions. Another possibility is to coat the sample surface with a conductive thin film to avoid charging problems. In this case the coating is made as thin as possible in order to be able to view topographical features. In this work the gas system was used to deposit Pt both as a protective coating and to avoid charging problems.

4.5 FIB/SEM workstation

In addition to the SEM and the FIB an FEI Strata DB 235M combined FIB/SEM system was used, mainly to produce TEM samples. It is a dual beam system, equipped with both an electron column and an ion column. The design and contrast mechanisms of the electron column and the ion column follow the description given in section 4.2 (SEM) and section 4.4 (FIB). The electron column is equipped with a FEG and the ion column with a liquid gallium source. The ion column is tilted 52° relative the electron column. The FIB/SEM is equipped with an Omniprobe micromanipulator and an electron and ion assisted Pt-deposition system. This makes *in-situ* liftout technology for TEM sample preparation possible, which will be described in section 4.7.4.

4.6 Transmission electron microscope (TEM)

The principle of the TEM is different from the SEM and the FIB, which have a lot of similarities. It is again charged particles, electrons, which are accelerated and directed towards the sample, but instead of being scattered back most of the electrons continue through the sample. This requires that the sample is electron transparent, which usually means that the sample should be less than 100 nm thick. A thin sample gives the opportunity to use analytical techniques with high spatial resolution, which increases the possibilities to get information about the microstructure and chemical composition. A Philips CM 200 FEG transmission electron microscope (TEM) was used in this work. It is equipped with a Link Isis EDX system. The software can be used for scanning transmission electron microscope (STEM) imaging, EDX spot analysis, EDX linescans and EDX mapping.

4.6.1 The design of the TEM

In a TEM the whole image is formed simultaneously. Fig. 4.8 shows a schematic drawing of a TEM. The electron sources are of the same types as in the SEM but the accelerating voltage is higher. The SEM is often operated at an accelerating voltage of 20 kV and the TEM at 200 kV. The electron gun forms, together with the condenser lenses, the illumination part of the microscope, below which the objective lens is situated. The objective lens forms the image of the specimen. The final parts are the projector lenses, which further magnifies the image, and the image recording system. Three apertures have key functions in the TEM. The first aperture, the condenser aperture, limits the beam divergence and beam load on the specimen. With the second aperture, the objective aperture, the image contrast is controlled. The third aperture, the selected area aperture, is located in the image plane of the objective lens and makes it possible to select small areas on the sample from which diffraction patterns can be obtained. For the same reason as in the SEM and FIB it is important to maintain high vacuum in the TEM.

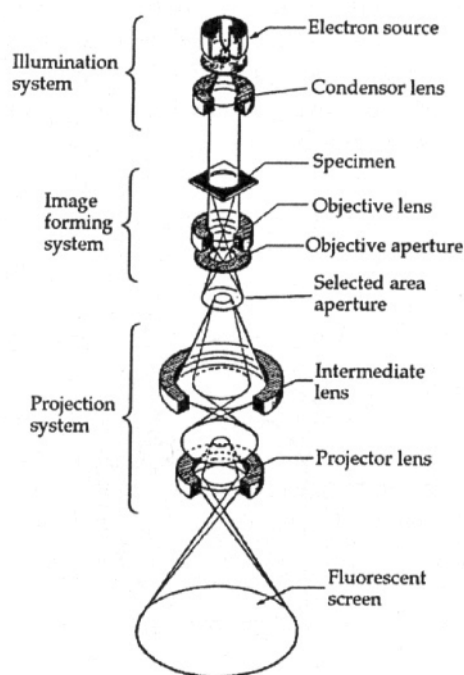


Figure 4.8: A schematic drawing of a TEM [44].

4.6.2 Imaging modes

Interaction of the high-energy electrons with the sample will make it possible to acquire information about chemical composition and the crystal structure. There is a wide range of techniques available to achieve this. For this work imaging, electron diffraction and chemical analysis by EDX have been used. If the investigated material is crystalline the majority of the transmitted electrons either go straight through or becomes scattered in discrete directions according to Bragg's law. This phenomenon will create a diffraction pattern in the focal plane of the objective lens. By inserting a selected area aperture and thereby limiting the region from which the electron pattern is obtained the diffraction pattern gives information about the crystal structure and lattice parameter in that region. This technique is known as selected area electron diffraction (SAED). In order to increase the resolution, to approximately 10 nm, convergent beam electron diffraction (CBED) could be employed. A converging incoming electron beam is then used, instead of parallel electron beams as for SAED, to illuminate a small region of the sample. The diffraction pattern will then consist of discs instead of spots as for SAED. The effect of electron diffraction is in addition used for imaging. By inserting an objective aperture only the transmitted electrons, bright field (BF) imaging, or only Bragg scattered electrons, dark field (DF) imaging, could be used. BF imaging is illustrated in Fig. 4.9a and DF imaging in 4.9b [44].

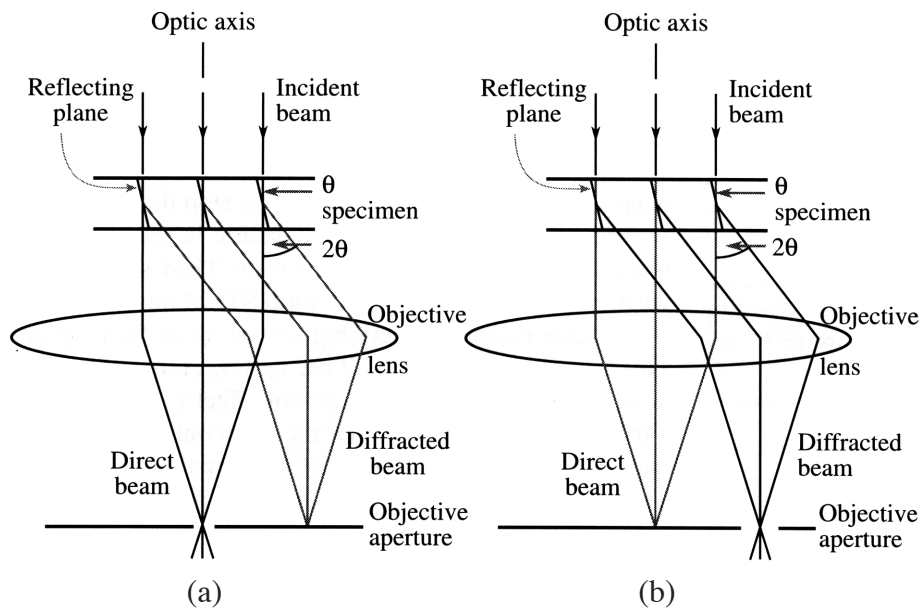


Figure 4.9: Diffraction contrast in TEM. Illustration of the electron beam paths for (a) bright field and (b) dark field imaging [44].

4.6.3 Scanning transmission electron microscope (STEM)

In order to characterize the chemical composition with high resolution the TEM was used in scanning transmission electron microscope (STEM) mode. In this mode the primary electron beam is focused and scanned over the electron transparent area on the sample.

STEM/EDX

The STEM/EDX analysis approximately works as in the SEM but with the difference that the thin TEM specimen increases the resolution to approximately 5 nm in the TEM compared to approximately 1 μm in the SEM, at an accelerating voltage of 20 kV. For quantification thin sample corrections are used instead of bulk corrections, as was described in section 4.2.2. For thin sample corrections the specimen thickness is often assumed to be thin enough so that absorption and fluorescence can be ignored, *i.e.* the A and F factors in the bulk correction (ZAF). This is known as the “thin foil criterion” [44]. However, modern EDX software use absorption corrections also for thin samples.

4.7 Specimen preparation

One of the most important parts of the experimental work is sample preparation. How to best prepare the sample in order to be able to study the microstructure is a difficult task. The different microscopes used in this work require different sample preparation techniques, which are described below.

4.7.1 Specimen preparation: FIB and SEM/EDX

For the surface morphology investigations of the oxide scales, for which both the FIB and the SEM were used, no sample preparation was required. However, in order to be able to investigate the oxide scale further, cross-sections of the oxide scales and the subjacent metal were ion milled with the FIB workstation.

One-sided cross-sections

Two different types of cross-sections were created. One type will be referred to as TEM samples, *i.e.* electron transparent cross-sections, see below. The other type will be referred to as one-sided cross-sections. These cross-sections are ion-milled only on one side, *i.e.* bulk samples with an ion-milled cross-section through the oxide scale and the subjacent metal. Two different techniques were used in order to create one-sided cross-sections of the oxide scale and the subjacent metal. When it was possible the samples were first cut with a low speed diamond saw in order to create cross-sections of central regions of the samples. The side on which the investigation was to be done was turned against the saw blade to avoid burrs damaging the oxide. The cut surface was then polished first with 240- and 600-mesh SiC paper and followed by 6 and 3 μm diamond paste. All the cut and polished slices were cleaned in an ultrasonic cleaner and stored in a desiccator. For the samples containing water-soluble species the low speed diamond saw was used without cutting fluid. The samples were then gently polished with 240- and 600-mesh SiC paper and cleaned by compressed air before FIB ion milling to avoid water-soluble species from being dissolved during the sample preparation step.

In order to prepare smooth cross-sections of the oxide scales the samples were milled with the FIB workstation. In Fig. 4.10a an example of a polished edge with an ion milled cross-section is shown in plan view. The finished cross-section after milling is shown in Fig. 4.10b where the sample has been tilted 45° to be able to image the cross-section. One important aspect is to mill cross-sections with the possibility to perform subsequent chemical analysis (SEM/EDX), *i.e.* to create a geometry so that BSEs from the cross-section do not hit the sides and create spurious X-rays. In order to produce a smooth cross-section surface the ion current used during the milling was lowered as the milling proceeded. A typical sequence of ion currents was 20 nA, 7 nA, 3 nA, 1 nA and 0.5 nA. For some of the cross-sections the probe currents 300 pA and 100 pA had to be used in order to get a smooth surface. The samples were then mounted with the one-sided cross-sections facing the electron beam in order to perform chemical analysis (SEM/EDX), see Fig. 4.11. The cross-section was positioned so that there was an open path to the EDX detector.

However, in some cases it was not appropriate to create cuts with the low speed saw in order to be able to mill cross-sections, *e.g.* when spallation occurred close to the cut edge. For those occasions another technique was used to create one-sided cross-sections. First a trench was milled beside the feature. The cross-section was then milled with 45° tilt relative the sample surface through the feature of interest, see

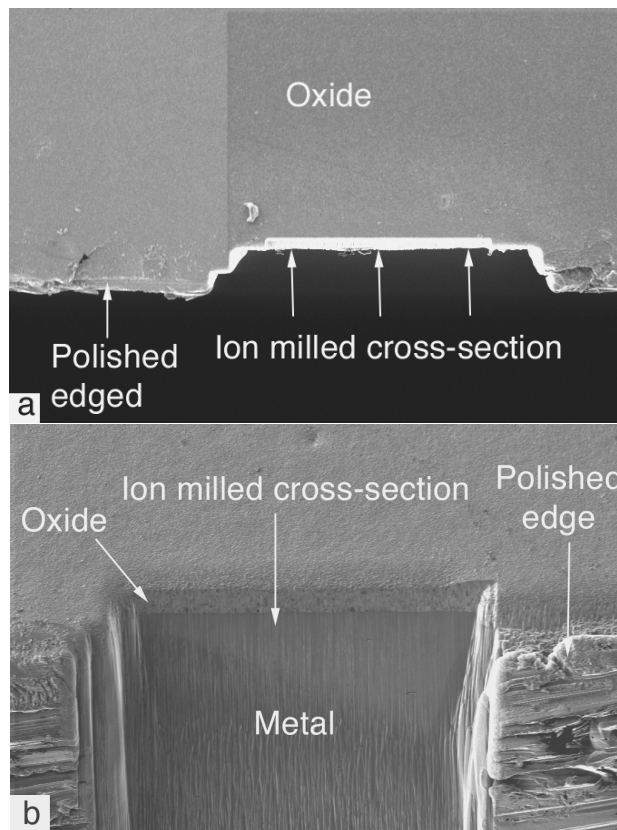


Figure 4.10: In (a) the polished edge is shown with an ion milled cross-section in top view and in (b) the finished cross-section is shown with a sample tilt of 30°. Both images are FIB images.

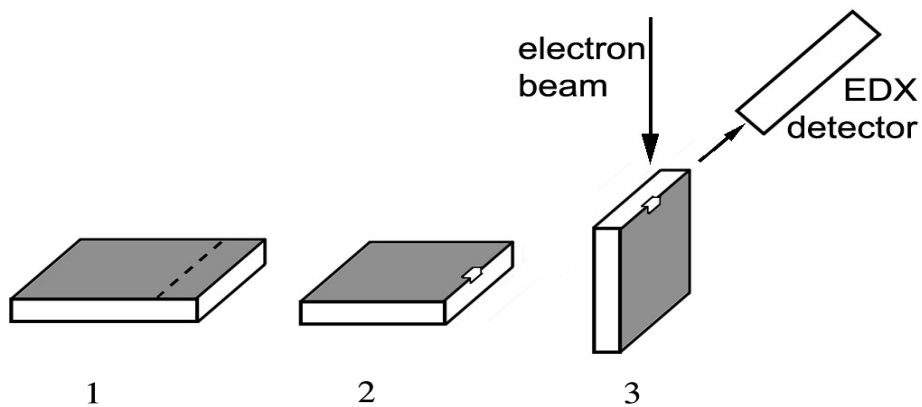


Figure 4.11: A schematic drawing of the sample preparation creating an ion-milled cross-section and the geometry used to perform chemical analysis (SEM/EDX) [45].

Fig. 4.12. This made it possible to perform chemical analysis (SEM/EDX) of the ion milled cross-section by mounting the sample in the SEM with 45° tilt, *i.e.* 0° tilt of the cross-section normal.

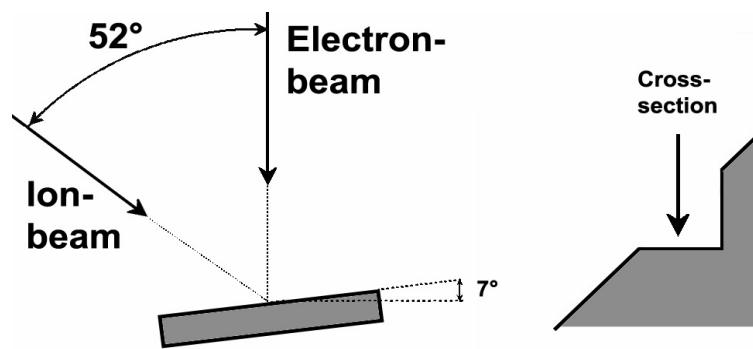


Figure 4.12: A schematic drawing of a cross-section milled with 45° tilt relative the sample surface. This made it possible to perform chemical analysis (SEM/EDX) of the ion milled cross-section by mounting the sample in the SEM with 45° tilt, i.e. 0° tilt of the cross-section normal [45].

4.7.2 Specimen preparation: ESEM *in-situ* exposures and analysis

To be able to compare furnace exposures with ESEM *in-situ* exposures the same sample preparation technique was used as for the furnace exposures. The samples were polished and then cleaned as described in section 4.1.1, with the exception that coupons with dimensions 4x4x2 mm³ had to be used in order to fit into the ESEM heating stage sample holder. For the final steps the samples were then cut with a low speed saw into coupons with dimensions 4x4x2 mm³ followed by polishing with 1 μm diamond paste. Only one side of the small samples was polished since only one side was analyzed during the *in-situ* study.

4.7.4 Specimen preparation: TEM and STEM/EDX

In order to prepare the TEM samples more work was required because of the demand of electron transparency. Two different techniques were used in order to create TEM samples: cutting and polishing together with FIB milling and the *in-situ* liftout technique performed in the FIB/SEM workstation. The liftout technique was used to create TEM samples of special features on the oxide scale, thin oxide scales or when water-soluble species were present.

TEM specimen preparation with the FIB workstation

In order to create a TEM sample in the FIB workstation an approximately 400 μm thick strip was cut from the coupon approximately 5 mm from the edge. It was mechanically polished until the thickness was approximately 150 μm. The next step was to punch 3 mm diameter discs from the strip. The different sample preparation steps are shown in Fig. 4.13. The discs were then polished down to a final thickness of approximately 50 μm using SiC paper 600 mesh and diamond paste 6 and 3 μm. During the final step the FIB workstation was used. The discs were placed in a

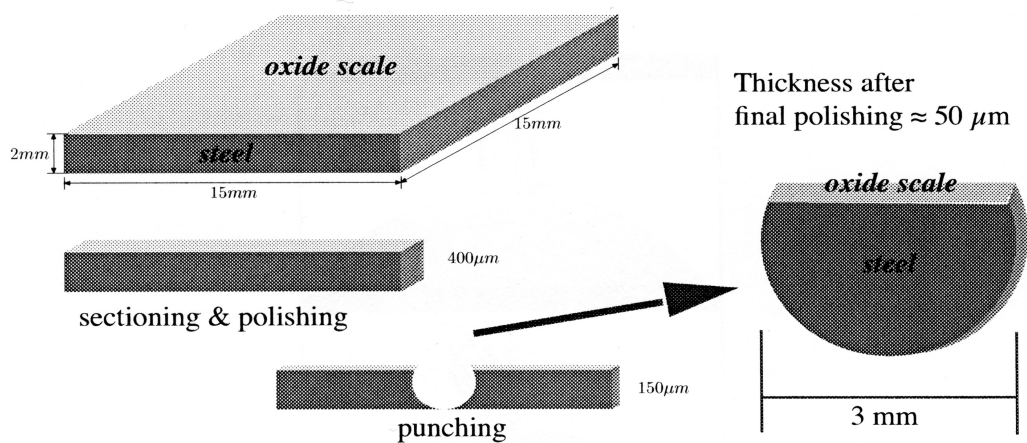


Figure 4.13: The different steps in the specimen preparation process. The top drawing shows a sample after exposure in the furnace. In the middle, a cut slice before grinding and polishing is drawn. The bottom part shows a polished slice from which a TEM disc has been punched out.

special holder that made it possible to mill away material from both sides of the disc in order to create an electron transparent membrane, see Fig. 4.14. In order to protect the oxide scale a $4\ \mu\text{m}$ thick Pt-layer was first deposited *in-situ* in the FIB onto the oxide scale to protect the top surface during ion milling. However, the outer part of the oxide is often damaged since the ion beam scans the target area before any Pt has been deposited. By comparing the results with other techniques, *e.g.* glow discharge optical emission spectroscopy (GDOES), the damaged layer is estimated to be less than 25 nm. In Fig. 4.15a a deposited Pt-strip on a disc is shown and in Fig. 4.15b the same disc is shown with a tilt of 30° after the coarse step milling in the FIB.

Caution has to be taken during the final part of the milling. If too high currents are used a thick amorphous layer can be created on the cross-section. A typical sequence of ion currents were: if the thickness was $10\ \mu\text{m}$ or more: 20 nA, if the thickness was less than $10\ \mu\text{m}$ and more than 2-4 μm : 3-7 nA, if the thickness was less than 2-4 μm

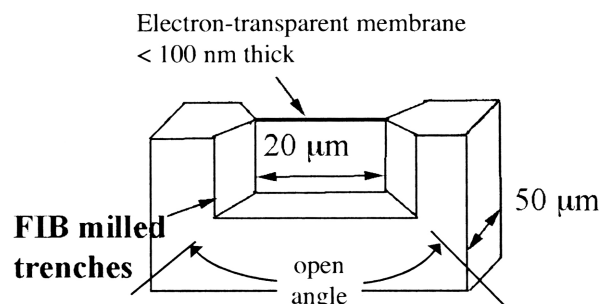


Figure 4.14: A schematic drawing of a FIB milled electron area (not drawn to scale).

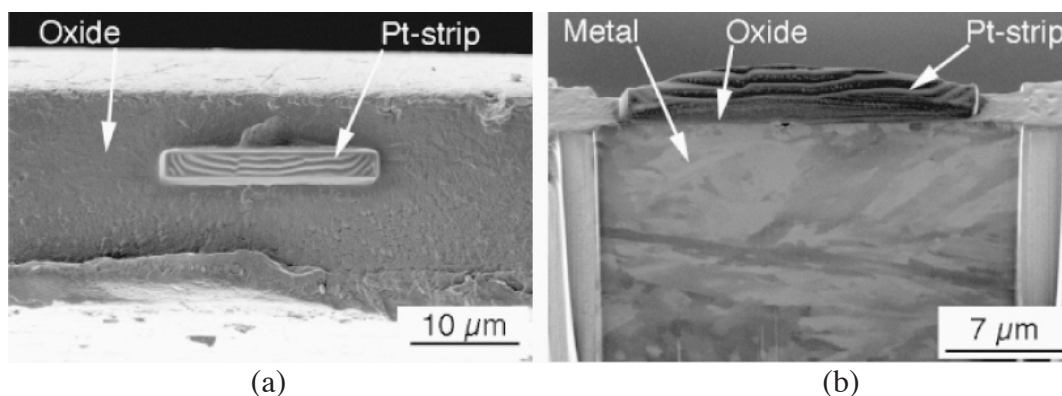


Figure 4.15: (a) A deposited Pt-strip on a disc. (b) The same disc is shown with a tilt of 30° after the coarse milling in the FIB.

and more than $0.5 \mu\text{m}$: 1 nA and for the final milling down to 100 nm: 500-100 pA. During the fine milling the sample was tilted approximately one degree in order to create a smooth electron transparent area with parallel sides.

TEM specimen preparation with the FIB/SEM workstation

The FIB/SEM workstation was used to produce TEM samples by the *in-situ* liftout technique. The *in-situ* liftout procedure was performed by first using the SEM column to choose a suitable position and to deposit an electron assisted protective Pt-layer, see Fig. 4.16a. The electron assisted Pt-deposited area protects the oxide scale and limits the damaged outer part of the oxide. This is an advantage when working with thin oxide scales. The next step was to deposit a thicker ion-assisted Pt-layer on top of the first Pt-layer, since ion assisted Pt-deposition is much faster. A high ion current, 20 nA, was then used to mill two trenches, one on each side of the Pt-protected area. The sample was then tilted 52° and ions were again used, ion current 5 nA, to mill away material beneath and on the sides of the specimen that was going to be lifted out, leaving it hanging on two bridges. A micromanipulator (Omniprobe) was then inserted and fastened to the specimen see Fig. 4.16b. After the bridges were milled away the stage was lowered and the liftout specimen was mounted to a 400-mesh Cu-grid, which had been cut in half, see Fig. 4.16c. The final steps were to cut loose the Omniprobe with ions, ion current 1 nA, and prepare a electron transparent area of the liftout specimen with the same technique as in the FIB workstation, see above. A finished electron transparent liftout sample is shown in Fig. 4.16d.

4.8 Complementary experimental techniques

Collaborators at the Department of Chemical and Biological Engineering at Chalmers University of Technology performed complementary analysis of the samples, mainly XRD. The basic concept of this technique will be described below.

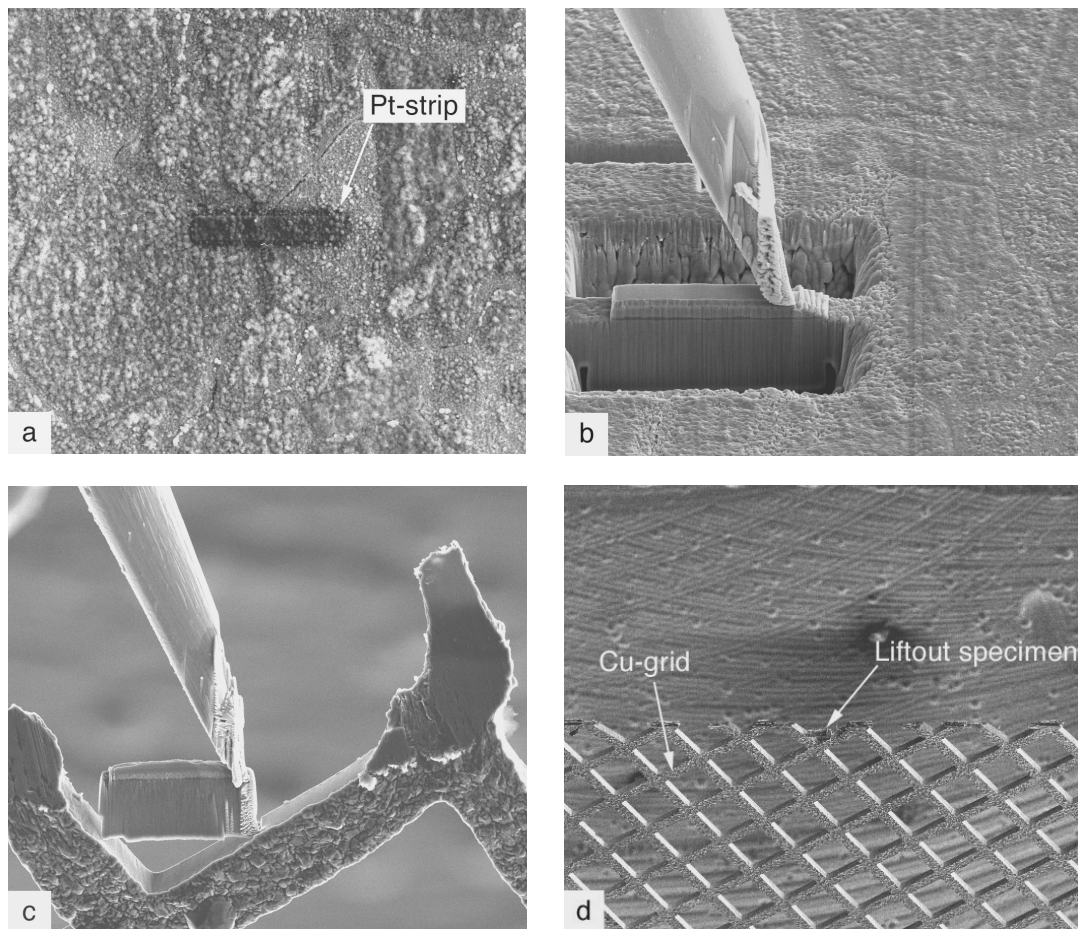


Figure 4.16: SEM micrographs of the liftout process in the FIB/SEM. In (a) the electron assisted Pt-deposited area is shown, before the ion assisted Pt had been deposited. The specimen that was going to be lifted out was milled free except for two bridges, leaving it hanging on those bridges. The next step was to insert the Omniprobe micromanipulator and fasten its tip to the specimen (b). After the bridges were milled away the stage was lowered and the liftout specimen was mounted to a 400-mesh prepared Cu-grid (c). In (d) the Cu-grid with the liftout specimen is shown in low magnification. The specimen is approximately 20 μm wide.

4.8.1 X-ray diffraction (XRD)

X-ray diffraction (XRD) gives information about the different crystalline phases present in the sample. It has a low lateral resolution and is a non-destructive technique. In connection to this work a Siemens D5000 X-ray diffractometer was used with two types of setups, *i.e.* Bragg-Brentano geometry and grazing incidence geometry. For XRD analysis an X-ray source, typically Cr or Cu, generates an X-ray beam with a discrete wavelength, which is directed towards the sample. The X-ray beam is then diffracted in discrete directions according to Bragg's law. The diffracted X-rays are detected in order to identify the crystal structure, *i.e.* to compare with a

database consisting of data from known crystal structures. Different setups of the incoming X-ray beam and the detector are possible. In Bragg-Brentano geometry both the X-ray source and the detector are symmetrically moved. This setup is the most common and is often used for bulk analysis. In order to be able to analyse a thin film, *e.g.* corrosion products, another setup can be used. In grazing incidence X-ray diffraction the X-ray source has a fixed angle relative to the sample, typically $0.1-5^\circ$, and the detector is scanned over different angles.

Chapter 5

Result and discussion

5.1 Summary of appended papers

Seven papers are included in this thesis. In paper I the effect of low levels of sulphur dioxide on the oxidation of iron is studied. Papers II to V investigate the impact of water vapour in the atmosphere at elevated temperatures, 500 to 900 °C, on iron and two stainless steels. In Paper VI and VII the effect of small KCl(s) additions on the oxidation of the stainless steel 304L is studied.

Paper I – The effect of traces of SO₂ on iron oxidation: A microstructural study

This paper documents the effect of low levels of sulphur dioxide on the microstructure of iron at 525 °C. Previous laboratory experiments showed a decreased oxidation rate in the presences of low levels of sulphur dioxide. To study this effect iron samples exposed to pure O₂, or O₂ with 100 ppm SO₂, for 1 or 24 hours at 525 °C were investigated. It was found that the oxide surface is considerably less porous and that early stages of whisker growth can be seen after one hour's exposure in the presence of SO₂. In pure oxygen the surface morphology of the oxide after 24 hours is very similar to that observed after one hour, while exposure for 24 hours in the presence of SO₂ produces extensive whisker growth. After one hour's exposure in O₂ the oxide layer mainly consists of two magnetite layers below a thin hematite layer. Both the two magnetite layers and the hematite layer grow with time. The inner, thinner layer of magnetite and the outer thicker magnetite is separated by a straight interface. Exposure in the presence of SO₂ results in a thinner less porous oxide scale with a considerably slower growing inner magnetite layer than in O₂. FeS forms as discrete grains in the inner magnetite layer while iron sulphate forms at the oxide surface. The

amount of sulphide at the metal/oxide interface is increased going from one hour to 24 hours of exposure. The inhibitive effect is attributed to iron sulphate that blocks active sites on the hematite surface, slowing down the formation of oxygen ions. This explains the strong inhibition of the inward growth of the duplex scale by SO_2 .

Paper II – An ESEM *in-situ* investigation of the influence of H_2O on iron oxidation at 500°C

The aim with this paper is to understand the initial growth of iron oxide at 500°C and the effect of different $\text{O}_2/\text{H}_2\text{O}$ mixtures by studying the oxide growth *in-situ* in the ESEM. Three different atmospheres, *i.e.* dry air, air with $\sim 1\%$ H_2O and almost pure H_2O , were therefore investigated during the first hour of oxidation. The ESEM *in-situ* exposure technique was in addition evaluated through a comparison with well-controlled reference furnace exposures.

It was found that several factors influence the growth rate. Some might increase the growth rate, while others, at the same time, can decrease the growth rate. Several characteristic features of the oxide scale microstructure, which may influence the growth rate, have been observed through a combination of experimental techniques, *i.e.* ESEM *in-situ* exposures and analysis, FIB and FSE imaging. The oxide consists of a layered oxide in all environments. The growth rate of the layered scale is in addition related to different metal grains in all environments. In dry and wet air a two-layered magnetite forms beneath a thin, fine-grained hematite layer, while only a two layered magnetite forms in H_2O . The two magnetite layers are separated by a straight interface, which is suggested to be the original metal surface. The inward grown magnetite is roughly one order of magnitude smaller than the outgrown layer, and has about the same grain size in all environments. The outward grown magnetite has more columnar grains, which are larger in H_2O than in dry and wet air.

The presence of low levels of water vapour (air with $\sim 1\%$ H_2O) produces a thicker hematite layer (compared to dry air), exhibiting a large number of whiskers on the surface. On the contrary, no hematite could be detected on scales formed in H_2O . These scales were thinner than the corresponding scales formed in dry and wet air. The slower growth rate in H_2O is suggested to be caused by the lower density of magnetite grain boundaries (larger grain size) in the outward growing magnetite scale and the low oxygen partial pressure in the chamber. Two types of pores form in the magnetite. Larger pores form in the inward growing magnetite layer and smaller pores form in the outward growing layer. The later pores are big and few in the middle, but the size decreases and the number increases with distance from the centre.

Thus, the experimental observations indicate that at least four different factors influence the local oxide growth rate: (i) the surface of the metal grain, (ii) the thickness of the hematite layer, (iii) the oxide grain size, and (iv) the exposure environment.

ESEM *in-situ* exposures and analysis was in addition shown to be a very powerful tool in order to study high temperature oxidation, especially if combined with FSE imaging prior to the exposures and FIB milling and imaging afterwards. The exposures were shown to have surprisingly high quality and reproducibility despite the fact that they are performed inside the microscope.

Paper III - Microstructure Investigation of Protective and Non-Protective Oxides on 11% Cr Steel

The impact of water vapour on the oxidation mechanisms of the ferritic/martensitic stainless steel X20 is in this paper studied at 600 °C. The X20 stainless steel is often used in power plants and is therefore exposed to water vapour containing environments. This study also enables a comparison between the behaviour of a ferritic/martensitic stainless steel and the behaviour of austenitic stainless steels in the presence of water vapour. A thin Cr-rich protective oxide formed in pure oxygen and in low flow rate when water vapour was present (O_2 with 40% H_2O) for 168 hours. The outmost part of the thin oxide scale was however depleted of Cr when water vapour was present due to the formation of $CrO_2(OH)_2(g)$. After longer exposure times (336 hours) or with higher flow rate in the presence of water vapour breakaway oxidation occurred. This resulted in a transformation from a thin Cr-rich oxide scale to a thick two-layered (inward and outward growing) oxide scale. The outward growing layer consisted of Fe-rich hematite $(Fe,Cr)_2O_3$ and the inward growing layer consisted of $(Fe,Cr)_3O_4$ spinel. It was shown that the transition from a thin protective Cr-rich oxide scale to non-protective Fe-rich oxide scale is faster, *i.e.* the entire surface is covered with thick oxide within a short time after the initiation of breakaway oxidation, for a ferritic/martensitic stainless steel than for a typical austenitic stainless steel. This can be attributed to the higher bulk diffusion rate through the ferritic structure and the higher density of faster diffusion paths (steel grain boundaries) in the ferritic/martensitic structure.

Paper IV - Microstructural investigation of the effect of water vapour on the oxidation of alloy 353MA at 700 and 900°C

In this study the impact of water vapour on the oxidation mechanisms of the austenitic stainless steel 353MA was investigated at 700 °C and 900 °C. The 353MA stainless steel is a commercial alloy designed to withstand oxidation at elevated temperatures. Like other high-alloyed austenitic Fe-Cr stainless steels designed for high temperature applications, it contains a high concentration of Cr and Ni. However, additions of Si and the reactive element Ce separate 353MA from conventional stainless steels. At 700 °C, 353MA forms a Cr-rich protective $(Fe,Cr)_2O_3$ oxide scale with some silica at the oxide/metal interface. Local breakaway oxidation occurs in H_2O/O_2 mixtures because the oxide scale is depleted in Cr due to the formation of $CrO_2(OH)_2(g)$. However, the microstructural investigation indicated that a Cr-rich healing layer forms beneath the Fe-rich oxide after some time. This is probably due to the high Cr/Fe ratio of 353MA. The behaviour at 900 °C was different. In spite of

the loss of Cr from the oxide scale breakaway oxidation did not occur, *i.e.* the oxide scale remained protective. The microstructural investigation showed a thick, almost continuous silica layer at the oxide/metal interface.

Paper V – Microstructural investigation of the effect of water vapour on the oxidation of the Si-containing FeCrNi steel 353MA at 900°C in oxygen

This paper investigates the corrosion behavior of steel 353MA at 900 °C in O₂ and in O₂ with 40% H₂O after 168 hours. A layered scale forms in dry O₂ as well as in O₂+H₂O environment. In both environments there is a discontinuous silica layer at the steel/oxide interface covered by a continuous chromia layer. The top part of the scale is made up of spinel oxide. In dry O₂ the spinel consists of “MnCr₂O₄” while “MnCr₂O₄”, “Mn₂CrO₄” and Fe-Ni rich spinel form in O₂+H₂O environment. The lateral distribution of Fe-Ni rich spinel is correlated to the grain structure of the steel, *i.e.*, some metal grains are covered by Cr-Mn rich spinel oxide, while others are covered by Fe-Ni rich spinel. The Ce levels were below the EDX detection limit. The silica layer at the metal/oxide interface may influence the oxidation but it can hardly act as a diffusion barrier because of its discontinuous nature. Water vapour strongly affects the scale microstructure, by causing chromia evaporation through the formation of CrO₂(OH)₂(g). However, it does not trigger an acceleration of corrosion during the time-span studied (168 hours). The protectiveness of the scale is attributed to the continuous chromia layer. Several combined factors is suggested to make the presence of a continuous chromia layer possible despite chromia evaporation: (i) The supply of chromium to the scale by diffusion in the steel is expected to increase even more rapidly with temperature than does chromia evaporation. (ii) The spinels formed at the oxide/gas interface are beneficial for oxidation behaviour in wet oxygen because it slows down chromia evaporation. (iii) The high Ni content in the alloy makes the conversion of the protective chromia to poorly protective hematite by chromia vaporization more difficult.

Paper VI – The influence of KCl on the corrosion of an austenitic stainless steel (304L) in oxidizing humid conditions at 600°C: A microstructural study

The objective of this paper is to study the impact of KCl on the corrosion behaviour of the austenitic stainless steel 304L at 600°C in 5% O₂ + 40 % H₂O + N₂. Especially, the breakdown of the protective oxide is investigated. This was done through a detailed microstructural characterization of the oxide scales formed after 1, 24 and 168 hours. The presence of KCl(s) causes a breakdown of most of the protective scale, even though it is not in direct contact with KCl(s) particles, already after 1 hour’s exposure. The remaining thin scale contains lower Cr levels than has been observed in corresponding scales formed in the absence of KCl. K₂CrO₄ particles were randomly distributed all over the scale. The particles are situated above the oxide scale and are not in direct contact with the subjacent metal. The breakdown of the protective scale is suggested to be caused primarily by the formation of K₂CrO₄,

depleting the protective oxide in chromium. In addition, chromia evaporation contributes to chromia depletion and breakdown of the protective scale. Very little or no transition metal chlorides was found after breakaway oxidation. Cl is suggested to play a minor role in the initial breakdown of the protective scale. The presence of KCl particles caused local rapid oxidation, which results in an outward growing Fe and Fe-Cr rich porous oxide.

Paper VII – Microstructural investigation of the influence of KCl on the corrosion of 304L exposed to 5% O₂ + N₂

This paper documents the effect of small amounts of KCl(s) on the microstructure of the austenitic stainless steel 304L at 600 °C in dry oxygen. The corrosion is strongly accelerated by small amounts of KCl(s). The initial step in the destruction of the protective oxide is considered to be the formation of potassium chromate (K₂CrO₄) particles close to the original KCl crystals already after 1 hour. Chromate formation depletes the protective oxide in chromium and converts it to poorly protective iron-rich oxide. The resulting scale is suggested to contain fast diffusion paths for Fe, O and Cl, giving rise to rapid corrosion. More Cl is expected to be present after longer times in exposures to dry oxygen compared to wet oxygen. This results in a multilayered oxide scale with bad adhesion.

5.2 Results from work in progress

Some results are part of ongoing work not yet published or in manuscript form. However, these results give complementary information to the results presented in the seven papers included in this thesis. A short summary of these results is therefore given below.

The effect of water vapour on the oxidation of iron

The ESEM *in-situ* study of the initial oxidation gives unique information about the oxidation mechanisms. However, no information about weight gain or longer exposure times was acquired with this technique. The effect of water vapour on the oxidation of iron is therefore in addition investigated through furnace exposures, together with weight gain measurements, in combination with ion and electron microscopy at 400, 500 and 600 °C. This study and the ESEM *in-situ* study give complementary information about the oxidation mechanisms of iron and the impact of water vapour. Preliminary results from the furnace exposures are in good agreement with the ESEM *in-situ* results. A difference in growth rate between different regions can be observed in both wet and dry oxygen, which is in accordance with the results from the ESEM *in-situ* exposures. An example of the surface morphology and the oxide thickness after 24 hours exposure in O₂ with 40% H₂O at 400 °C is shown in Fig. 5.1. The phenomenon with different growth rate on different regions was in the ESEM *in-situ* work (Paper II) shown to be related to the underlying metal grains. Low levels of water vapour in the atmosphere causes, as in the *in-situ* exposures, whisker growth, see Fig. 5.1.

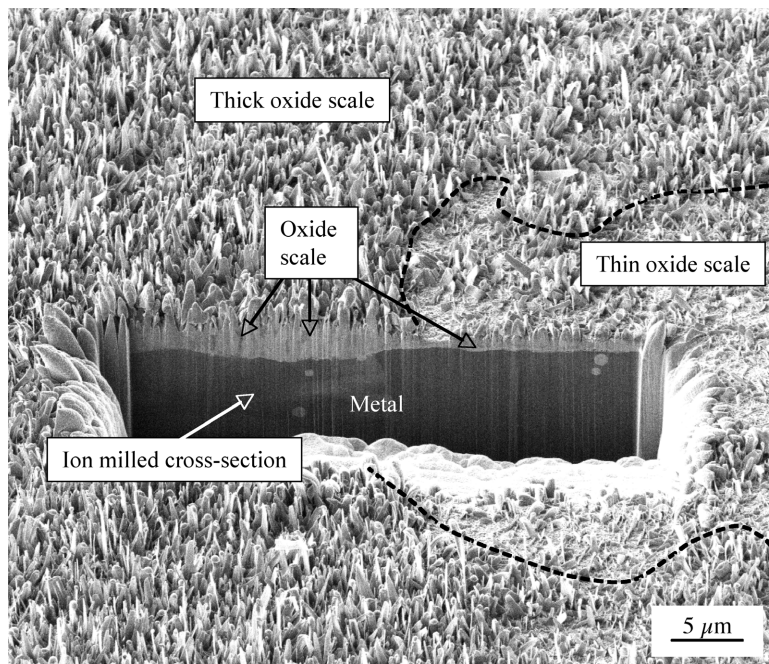


Figure 5.1: FIB image of an ion milled cross-section on iron exposed for 24 hours in O₂ with 40% H₂O at 400 °C.

The effect of water vapour on the oxidation of chromium

The effect of water vapour on the oxidation of chromium is investigated in order to better understand the effect of water vapour on stainless steels. This work is mainly aimed to study the mechanism of chromium evaporation by the presence of water vapour at medium temperatures (600-700 °C). The equilibrium partial pressure of CrO₂(OH)₂ is measured on metallic chromium and on chromia pellets. The influence of water vapour on the scale microstructure is investigated by electron and ion microscopy. The preliminary results show a difference in oxide growth rate between different metal grains, which is in agreement with the ESEM *in-situ* study (Paper II) and the preliminary results from the iron study (furnace exposures). An example of the surface morphology and the oxide thickness after 24 hours exposure in dry O₂ at 700 °C is shown in Fig. 5.2.

The effect of water vapour on the oxidation of Sanicro 28

In order to further understand the effect of water vapour another highly alloyed austenitic stainless steel is being investigated, Sanicro 28. It contains high levels of Cr and Ni and resembles 353MA except that it has no Ce and a lower Si content. The effect of water vapour is studied at 600 and 800 °C. Preliminary results from the study at 800 °C gives further information about silica at the metal/oxide interface, which was observed on 353MA. Silica forms at the oxide/metal interface also on Sanicro 28 even though the content in the alloy is lower than in 353MA. The results shows that

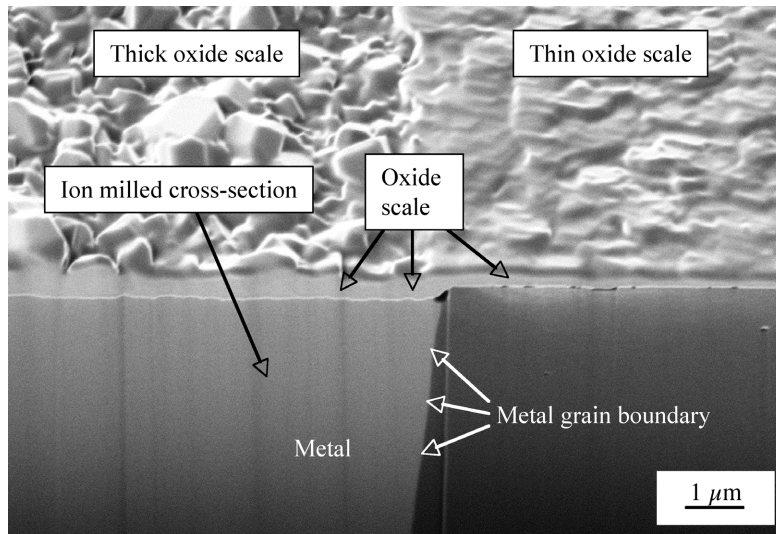


Figure 5.2: FIB image of an ion milled cross-section on chromium exposed for 24 hours in dry O_2 at 700 °C.

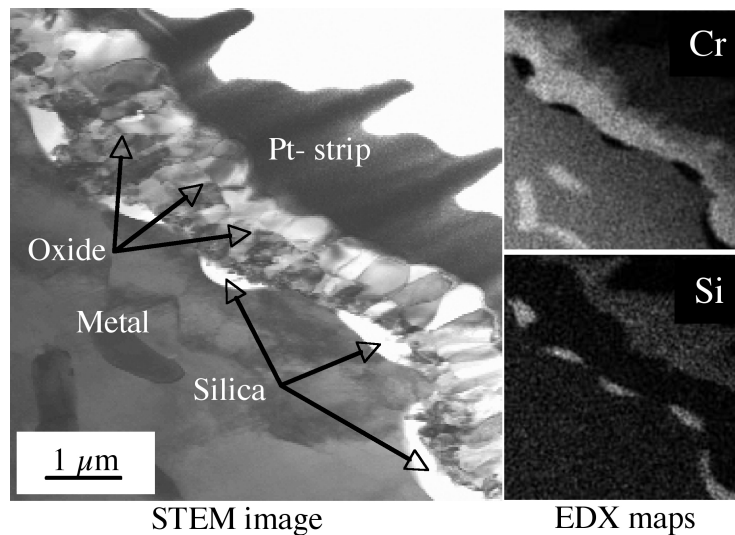


Figure 5.3: STEM image and STEM/EDX maps of Sanicro 28 exposed for 168 hours in O_2 with 40% H_2O at 800 °C. Silica regions can be seen at the oxide/metal interface.

silica forms a thin, more continuous layer after short exposure time (24 hours) while a thicker, discontinuous layer can be found after longer exposure times (168 hours) at 800 °C, see Fig. 5.3. A strong temperature dependence of this phenomenon could in addition be observed. At 600 °C (Sanicro 28) and 700 °C (353MA) only a thin, almost continuous Si rich layer could be observed after 168 hours while at 800 °C (Sanicro 28) and 900 °C (353MA) a thicker discontinuous silica layer was observed after 168 hours.

5.3 Future work

The results from the work performed within the scope of this thesis have provided new knowledge concerning the oxidation mechanisms of iron and some stainless steels. However, the results have in addition raised new questions regarding the oxidation mechanisms. In this section a few suggestions are given for future work based on the results presented in this thesis.

The effect of low levels of sulphur dioxide on the oxidation mechanisms on other metals and alloys could in addition be studied. Can low levels of sulphur dioxide generally slow down the oxidation rate? Detailed microstructural investigations of different metals and alloys exposed to environments with and without low levels of sulphur dioxide would therefore be important to perform.

The effect of water vapour at elevated temperatures has been extensively studied on Fe, Cr and on commercial stainless steels with different chromium content and microstructure. In order to further understand the fundamental mechanisms, *i.e.* how the Cr content in the alloy together with Cr evaporation is coupled to the formation of a Cr-rich protective oxide scale, model alloys could be studied. Commercial alloys contain many elements that could affect the oxidation behaviour. Therefore it would be valuable to study the effect of water vapour on model alloys with different Fe/Cr ratios in order to better understand the oxidation mechanisms.

Water vapour has been shown to increase the oxidation rate on stainless steels, while the low levels of sulphur dioxide have been shown to decrease the oxidation rate on iron. Preliminary studies have shown that these effects can be combined to limit the effect of water vapour on stainless steels. In order to better understand this phenomenon an investigation of the impact of the combined effect of these two species on the microstructure would be valuable.

The presence of KCl(s) has been shown to increase the oxidation rate of stainless steels. The role of alkali and chlorine in the oxidation mechanisms can be further investigated by studies of other alkali salts than KCl, *e.g.* K_2CO_3 and K_2SO_4 . The effect of HCl should in addition be investigated. Detailed microstructural investigations of stainless steels exposed to environments with and without these species would therefore be important to perform.

ESEM *in-situ* exposures and analysis have been shown to be very powerful in order to study high temperature oxidation, especially if combined with FSE imaging and FIB milling. This combination of techniques would be valuable to use in order to further study other systems, *e.g.* the effect of different alkali salts on stainless steels.

The SEM investigations can in addition be upgraded towards higher resolution by the possibility to perform scanning transmission electron microscopy (STEM) on thin foil samples in the SEM. This offers possibilities to perform more analyses in the SEM before using the more time demanding TEM.

In order to determine the crystal structures present in the oxide scales electron backscattered diffraction (EBSD) can be performed in the SEM. The spatial resolution is rather good (≤ 100 nm) and the number of analysed grains can be high (compared to TEM) due to the use of automated software for diffraction pattern indexing. However, the EBSD technique requires very smooth cross-sections for analysis. The FIB workstation could be used, to create such cross-sections. Another possibility would be to use a broad ion beam (BIB). The BIB technique would have an advantage over the FIB technique since it gives the possibility to create much wider cross-sections for analysis.

One of the most important factors for this work is the combination of well-controlled exposures and a microstructural investigation performed by advanced electron and ion microscopy. This has been possible through the collaboration within the HTC centre and the SSF programme. It is important to continue this type of collaboration in order to acquire further knowledge within this research field.

Acknowledgements

I would like to thank a number of people who in different ways contributed to the work presented in this thesis.

My supervisor Assoc. Prof. Mats Halvarsson for leading me through this work.

My co-authors for the constructive cooperation that resulted in the papers included: Anders Järtnäs, Bagas Pujilaksono, Fang Liu, Henrik Asteman, Jan Froitzheim, Jesper Pettersson, Jun Eu Tang, John Ågren, Karin Segerdahl, Samuel Hallström and Sead Canovic.

Assoc. Prof. Jan-Erik Svensson and Prof. Lars-Gunnar Johansson at the Department of Chemical and Biological Engineering for interesting and fruitful discussions and a good cooperation.

Fang Liu for teaching me many of the instruments and for her unselfish help and support throughout this work.

Technical/administrative staff of the Microscopy and Microanalysis group: Dr. Anders Kvist for technical support with the instruments; Ola Löfgren, for great computer support; Birgitta Castedal for supporting me with administrative details.

All the past and present members of the Microscopy and Microanalysis group for offering a nice working environment.

All the “chemists” (past and present PhD students at the Department of Chemical and Biological Engineering) for contributing to the nice working environment.

All other friends and colleagues who supported me and made this possible, especially Anders Olofsson.

My parents and my parents in law for supporting me through out this work.

Finally, my deepest thanks go to my wife Annika for all her love and support.

Financial support from the Swedish High Temperature Corrosion centre (HTC), the Swedish National Research Council (VR) and the Swedish Foundation for Strategic Research (SSF) Materials Research Programme “Mechanisms of creep and oxidation of high performance alloys” (CROX) are gratefully acknowledged.

References

1. Riedl, R., et al. *Corrosion in Fire Tube Boilers of Biomass Combustion Plants*. in *China International Corrosion Control Conference '99*. 1999. Beijing, China: China Chemical Anticorrosion Technology Association (CCATA).
2. Järdnäs, A., *The Influence of SO₂ on the High Temperature Corrosion of Fe and Fe-Cr Alloys*. 2005, Chalmers University of Technology: Gothenburg.
3. Asteman, H., *Water Vapour Induced Active Oxidation of Stainless Steel*, in *Department of Chemistry*. 2002, Göteborg University: Göteborg.
4. Tang, J.E., *The influence of water vapour on the oxidation behaviour of high temperature materials*, in *Department of Experimental Physics*. 2004, Chalmers University of Technology: Göteborg.
5. Spiegel, M., C. Schroer, and H.J. Grabke, *Corrosion of High Alloy Steels and Fe-Cr-Alloys Beneath Deposits from Waste Incinerator Plants*. Materials Science Forum, 1997. **251-254**: p. 527-534.
6. Grabke, H.J., E. Reese, and M. Spiegel, *The Effects of Chlorides, Hydrogen Chloride and Sulfur dioxide in the Oxidation of Steels Below deposits*. Corrosion Science, 1995. **37**(7): p. 1023-1043.
7. Michelsen, H.P., et al., *Deposition and High Temperature Corrosion in a 10 MW Straw Fired Boiler*. Fuel Processing Technology, 1998. **54**: p. 95-108.
8. Nielsen, H.P., F.J. Frandsen, and K. Dam-Johansen, *Lab-Scale Investigation of High-Temperature Corrosion Phenomena in Straw-Fired Boilers*. Energy & Fuels, 1999. **13**: p. 114-1121.
9. Honeycombe, R.W.K. and H.D.K.H. Bhadeshia, *Steels: Microstructure and Properties*. second edition ed. 1995.
10. Basu, S.N. and G.J. Yurek, *Effect of Alloy Grain Size and Silicon Content on the Oxidation of Austenitic Fe-Cr-Ni-Mn-Si Alloys in pure O₂*. Oxidation of Metals, 1991. **36**(3/4): p. 281-315.
11. Mikkelsen, L., S. Linderoth, and J.B. Bilde-Sorensen. *The Effect of Silicon Addition on the High Temperature Oxidation of a Fe-Cr Alloy*. in *6th International Symposium on High-Temperature Corrosion and Protection of Materials*. 2004. Les Embiez, France.

12. Wouters, Y., et al. *Oxygen and Water Vapour Oxidation of 15Cr Ferritic Stainless Steels with Different Silicon Contents*. in *6th International Symposium on High-Temperature Corrosion and Protection of Materials*. 2004. Les Embiez, France.
13. Hou, P.Y. and J. Stringer, *The Effect of Reactive Element Addition on the Selective Oxidation Growth and Adhesion of Chromia Scales*. *Materials Science and Engineering*, 1995. **A202**: p. 1-10.
14. Pint, B.A., *Experimental Observations in Support of the Dynamic-Segregation Theory to Explain the Reactive-Element Effect*. *Oxidation of Metals*, 1996. **45**(1/2): p. 1-37.
15. Whittle, D.P. and J. Stringer, *Improvement in Properties: Additives in Oxidation Resistance*. *Phil. Trans. R. Soc. Lond. A*, 1980. **295**: p. 309-329.
16. Stringer, J., *The Reactive Element Effect in High-temperature Corrosion*. *Materials Science and Engineering*, 1989. **A120**: p. 129-137.
17. Wagner, C., *Beitrag zur Theorie des Anlaufvorgangs*. *Z. Physicalische chemie*, 1933. **B21**: p. 25-41.
18. Birks, N. and G.H. Meier, *Introduction to High Temperature Oxidation of Metals*, ed. E. Arnold. 1983, London.
19. Kofstad, P., *High Temperature Corrosion*. 1988, London and New York: Elsevier Applied Science Publishers Ltd.
20. Khanna, A.S., *High Temperature and Corrosion*. *Materials Park*, ed. A. International. 2002.
21. Ebbinghaus, B.B., *Thermodynamics of Gas Phase Chromium Species: The Chromium Oxides, the Chromium Oxyhydroxides, and Volatility calculations in Waste Incineration Processes*. *Combustion and Flame*, 1993. **93**: p. 119-137.
22. Chen, R.Y. and W.Y.D. Yuen, *Review of the High-Temperature Oxidation of Iron and Carbon Steels in Air or Oxygen*. *Oxidation of Metals*, 2003. **59**: p. 433-468.
23. Segerdahl, K., *The Breakdown of the Protective Oxide on 11% Chromium Steel*, in *Department of Environmental Inorganic Chemistry*. 2003, Chalmers University of Technology: Göteborg.
24. Stott, F.H., G.C. Wood, and J. Stringer, *The Influence of Alloying Elements on the Development and Maintainance of Protective Scales*. *Oxidation of Metals*, 1995. **44**(1/2): p. 113-145.

25. Amy, S. and P. Vangeli. *Water Vapour Effect on the High Temperature Resistant Grades*. in *EUROCORR 2001*. 2001. Italy.
26. Flatley, T. and N. Birks, *Oxidation of iron in atmospheres containing sulphur dioxide*. *Journal of The Iron and Steel Institute*, 1971: p. 523-533.
27. Giggins, C.S. and F.S. Pettit, *Corrosion of Metals and Alloys in Mixed Gas Environments at Elevated Temperatures*. *Oxidation of Metals*, 1980. **14**(5): p. 363-413.
28. Mrowec, S., *The problem of sulphur in high-temperature corrosion*. *Oxidation of Metals*, 1995. **44**(1/2): p. 177-209.
29. Gesmundo, F., *Mechanism of the simultaneous formation of oxide and sulfide at the scale surface during the oxidation of a pure metal in mixed atmospheres*. *Oxidation of Metals*, 1979. **13**(3): p. 237-245.
30. Young, D.J. and S. Watson, *High-Temperature Corrosion in Mixed Gas Environments*. *Oxidation of Metals*, 1995. **44**(1/2): p. 239-264.
31. Rahmel, A. and J. Tobolski, *Einfluss von Wasserdampf und Kohlendioxyd auf die Oxydation von Eisen in Sauerstoff bei Hohen Temperaturen*. *Corrosion Science*, 1965. **5**: p. 333-346.
32. Tuck, C.W., M. Odgers, and K. Sachs, *Oxidation of iron at 950.deg. in oxygen/water vapor mixtures*. *Corrosion Science*, 1969. **9**: p. 271.
33. Fujii, C.T. and R.A. Meussner, *The Mechanism of the High-Temperature Oxidation of Iron-Chromium Alloys in Water Vapor*. *J. Electrochemical Society*, 1964. **111**(11).
34. Thiele, M., et al., *Corrosion Behaviour of Ferritic and Austenitic Steels in the Simulated Combustion Gases of Power Plants Fired with Hard Coal and Brown Coal*. *VGB Kraftwerkstechnik*, 1997. **77**(2): p. 129-134.
35. Quadackers, W.J. and P.J. Ennis. *The Oxidation Behaviour of Ferritic and Austenitic Steels in Simulated Power Plant Service Environments*. in *Materials for Advanced Power Engineering 1998*. 1998. Liege.
36. Hultquist, G., et al., *Self-Repairing Metal Oxides*. *Oxidation of Metals*, 2001. **56**(3/4).
37. Hultquist, G., B. Tveten, and E. Hörnlund, *Hydrogen in Chromium: Influence on the High-Temperature Oxidation Kinetics in H₂O, Oxide-Growth Mechanisms, and Scale Adherence*. *Oxidation of Metals*, 2000. **54**(1/2): p. 1-10.

38. Pettersson, J., *Alkali Induced Corrosion of 304L*, in *Department of Chemical and Biological Engineering*. 2005, Chalmers University of Technology: Gothenburg.
39. Montgomery, M. and A. Karlsson, *In-situ corrosion investigation at Masnedö CHP plant - a straw-fired power plant*. *Materials and Corrosion*, 1999. **50**: p. 579-584.
40. Lee, S.Y. and M.J. McNallan, *Formation of Condensed Chlorides During Mixed Oxidation Chlorination of Iron at 1000-K*. *Corrosion*, 1991. 47(11): p. 868-874.
41. Shinata, Y., *Accelerated Oxidation Rate of Chromium Induced by Sodium Chloride*. *Oxidation of Metals*, 1987. **27**(5/6): p. 315-332.
42. Pettersson, C., *The High Temperature Corrosion of Alloy Sanicro 28*, in *Department of Chemical and Biological Engineering*. 2006, Chalmers University of Technology: Gothenburg.
43. Goldstein, J., *Scanning Electron Microscopy and X-Ray Microanalysis*. Third Edition ed. 2003.
44. Williams, D.B. and C.B. Carter, *Transmission Electron Microscopy*. 1996, New York: Plenum Press.
45. Froitzheim, J., *Microstructural investigation of the influence of KCl on the high temperature corrosion of 304L*, in *Department of Applied Physics*. 2005, Chalmers University of Technology: Gothenburg.